



1 Global modelling of soil carbonyl sulfide exchanges

2 Camille Abadie¹, Fabienne Maignan¹, Marine Remaud¹, Jérôme Ogée², J. Elliott Campbell³,
3 Mary E. Whelan⁴, Florian Kitz⁵, Felix M. Spielmann⁵, Georg Wohlfahrt⁵, Richard Wehr⁶, Wu
4 Sun⁷, Nina Raoult¹, Ulli Seibt⁸, Didier Hauglustaine¹, Sinikka T. Lennartz^{9,10}, Sauveur
5 Belviso¹, David Montagne¹¹ and Philippe Peylin¹.

6 ¹Laboratoire des Sciences du Climat et de l'Environnement, LSCE/IPSL, CEA-CNRS-UVSQ, Université Paris-
7 Saclay, Gif-sur-Yvette, France

8 ²INRA, UMR 1391 ISPA, 33140 Villenave d'Ornon, France

9 ³Sierra Nevada Research Institute, University of California, Merced, California 95343, USA

10 ⁴Department of Environmental Sciences, Rutgers University, New Brunswick, NJ 08901, USA

11 ⁵Department of Ecology, University of Innsbruck, Innsbruck, 6020, Austria

12 ⁶Center for Atmospheric and Environmental Chemistry, Aerodyne Research, Inc., Billerica, Massachusetts, 01821,
13 USA.

14 ⁷Department of Global Ecology, Carnegie Institution for Science, Stanford, CA 94305, USA

15 ⁸Department of Atmospheric & Oceanic Sciences, University of California Los Angeles, California 90095, USA

16 ⁹Institute of Chemistry and Biology of the Marine Environment, University of Oldenburg, 26129 Oldenburg,
17 Germany

18 ¹⁰Department of Earth, Atmospheric and Planetary Sciences, Massachusetts Institute of Technology, Cambridge,
19 02139, MA, USA

20 ¹¹AgroParisTech, INRAE, Université Paris-Saclay, UMR ECOSYS, 78850 Thiverval-Grignon, France

21

22 *Correspondence to:* Camille Abadie (camille.abadie.research@gmail.com)

23 **Abstract.** Carbonyl sulfide (COS) is an atmospheric trace gas of interest for C cycle research because COS uptake
24 by continental vegetation is strongly related to terrestrial gross primary productivity (GPP), the largest and most
25 uncertain flux in atmospheric CO₂ budgets. However, to use atmospheric COS budgets as an additional tracer of
26 GPP, an accurate quantification of COS exchange by soils is also needed. At present, the atmospheric COS budget
27 is unbalanced globally, with total COS flux estimates from oxic and anoxic soils that vary between -409 and -104
28 GgS yr⁻¹. This uncertainty hampers the use of atmospheric COS concentrations to constrain GPP estimates through
29 atmospheric transport inversions. In this study we implemented a mechanistic soil COS model in the ORCHIDEE
30 land surface model to simulate COS fluxes in oxic and anoxic soils. Evaluation of the model against flux
31 measurements at 7 sites yields a mean root mean square deviation of 1.6 pmol m⁻² s⁻¹, instead of 2 pmol m⁻² s⁻¹
32 when using a previous empirical approach that links soil COS uptake to soil heterotrophic respiration. The new
33 model predicts that, globally and over the 2009-2016 period, oxic soils act as a net uptake of -126 GgS yr⁻¹, and
34 anoxic soils are a source of +96 GgS yr⁻¹, leading to a global net soil sink of only -30 GgS yr⁻¹, i.e., much smaller
35 than previous estimates. The small magnitude of the soil fluxes suggests that the error in the COS budget is
36 dominated by the much larger fluxes from plants, oceans, and industrial activities. The predicted spatial
37 distribution of soil COS fluxes, with large emissions in the tropics from oxic (up to 68.2 pmol COS m⁻² s⁻¹) and
38 anoxic (up to 36.8 pmol COS m⁻² s⁻¹) soils, marginally improves the latitudinal gradient of atmospheric COS
39 concentrations, after transport by the LMDZ atmospheric transport model. The impact of different soil COS flux
40 representations on the latitudinal gradient of the atmospheric COS concentrations is strongest in the northern
41 hemisphere. We also implemented spatio-temporal variations of near-ground atmospheric COS concentrations in
42 the modelling of biospheric COS fluxes, which helped reduce the imbalance of the atmospheric COS budget by
43 lowering COS uptake by soils and vegetation globally (-10% for soil, and -8% for vegetation with a revised mean
44 estimate of -576 GgS y⁻¹ over 2009-2016). Sensitivity analyses highlighted the different parameters to which each



45 soil COS flux model is the most responsive, selected in a parameter optimization framework. Having both
46 vegetation and soil COS fluxes modelled within ORCHIDEE opens the way for using observed ecosystem COS
47 fluxes and larger scale atmospheric COS mixing ratios to improve the simulated GPP, through data assimilation
48 techniques.

49 **1 Introduction**

50 Carbonyl sulfide (COS) has been proposed as a tracer for constraining the simulated Gross Primary Productivity
51 (GPP) in Land Surface Models (LSMs) (Launois et al., 2015; Remaud et al., 2021; Campbell et al., 2008). COS is
52 an atmospheric trace gas that is scavenged by plants at the leaf level through stomatal uptake and irreversibly
53 hydrolyzed in a reaction catalyzed by the enzyme Carbonic Anhydrase (CA) (Protoschill-Krebs et al., 1996). This
54 enzyme also interacts with CO₂ inside leaves. COS and CO₂ follow a similar pathway from the atmosphere to the
55 leaf interior. However, while CO₂ is also released during respiration, plants generally do not emit COS (Montzka
56 et al., 2007; Sandoval-Soto et al., 2005; Wohlfahrt et al., 2012). To infer GPP at the regional scale using COS
57 observations, modelers can use measurements of ecosystem COS fluxes directly, or measurements of atmospheric
58 COS concentrations combined with an atmospheric transport inversion model, provided all COS flux components
59 are taken into account. In both cases, net soil COS flux estimates are needed, as well as a functional relationship
60 between GPP and COS uptake by foliage.

61 One important limitation for using COS as a tracer for GPP is the uncertainty that remains on the COS budget
62 components. Several atmospheric transport inversion studies have suggested that a COS source located over the
63 tropical oceans and estimated between 700 and 1100 GgS yr⁻¹ was missing to close the contemporary COS budget
64 (Berry et al., 2013; Glatthor et al., 2015; Kuai et al., 2015). This hypothesis of a strong oceanic source has not
65 been substantiated by in situ COS and CS₂ measurements in sea waters (Lennartz et al., 2017, 2020, 2021), except
66 by Davidson et al. (2021) that invoke an oceanic source of 600 ± 400 GgS yr⁻¹ based on direct measurements of
67 sulfur isotopes. Clearly, an accurate characterization of all flux components of the atmospheric COS budget is still
68 needed. In particular, the contribution of soils to the COS budget is poorly constrained and improved estimates of
69 their contribution may therefore provide clues to the attribution of the missing source.

70 A distinction is usually made between oxic soils that mainly absorb COS, and anoxic soils that emit COS (Whelan
71 et al., 2018). Regarding COS uptake, COS diffuses into the soil, where it is hydrolyzed by CA contained in soil
72 microorganisms such as fungi and bacteria (Smith et al., 1999). It is to be noted that COS can also be consumed
73 by other enzymes, like nitrogenase, CO dehydrogenase, or CS₂ hydrolase (Smith and Ferry, 2000; Masaki et al.,
74 2021), but these enzymes are less ubiquitous than CA. The rate of uptake varies with soil type, temperature, and
75 soil moisture (Kesselmeier et al., 1999; VanDiest et al. 2007; Whelan et al., 2016). With high temperature or
76 radiation, soils were also found to emit COS through thermal or photo degradation processes (Kitz et al., 2017,
77 2020; Whelan and Rhew, 2015; Whelan et al., 2016, 2018). Although such COS emissions can be large in some
78 conditions, they are usually neglected in current figures of the atmospheric COS budget.

79 Using the empirical relationship between soil COS uptake and soil respiration by Yi et al. (2007), Berry et al.
80 (2013) provided new global estimates of COS uptake by oxic soils. Launois et al. (2015) proposed another
81 empirical model, linking oxic soil COS uptake to H₂ deposition based on the correlation between these two
82 processes observed at Gif-sur-Yvette (Belviso et al., 2013). Models with a physical representation of the involved
83 processes are also available. Sun et al. (2015) proposed such a mechanistic model including COS diffusion and



84 reactions within a layered soil. Ogée et al. (2016) also developed a mechanistic model including both COS uptake
85 and production, with steady-state analytical solutions in homogeneous soils. When including such models in an
86 LSM, the challenge is to spatialize them, which requires new variables or parameters not readily available at the
87 global scale but inferred from field or lab experiments.

88 In this study, our goal is to provide and evaluate new global estimates of net soil COS exchange. To this end:

- 89 i. We implemented an empirical-based and a mechanistic-based soil COS model in the ORCHIDEE
90 LSM;
- 91 ii. We evaluated the soil COS models at seven sites against in situ flux measurements;
- 92 iii. We estimated soil contributions to the COS budget at the global scale;
- 93 iv. We transported all COS sources and sinks using an atmospheric model and evaluated the
94 concentrations against measurements of the National Oceanic and Atmospheric Administration
95 (NOAA) air sampling network.

96 2 Methods

97 2.1 Description of the models

98 2.1.1 The ORCHIDEE Land Surface Model

99 The ORCHIDEE Land Surface Model is developed at the Institut Pierre Simon Laplace (IPSL). The model version
100 used here is the one involved in the 6th Coupled Model Inter-comparison Project (CMIP6) (Boucher et al., 2020;
101 Cheruy et al., 2020). ORCHIDEE computes the carbon, water and energy balances over land surfaces. It can be
102 run at the site level or at the global scale. Fast processes such as soil hydrology, photosynthesis and respiration are
103 computed at a half-hourly time step. Other processes such as carbon allocation, leaf phenology and soil carbon
104 turnover are evaluated at a daily time step. Plant species are classified into 14 Plant Functional Types (PFTs),
105 according to their structure (trees, grasslands, croplands), bioclimatic range (boreal, temperate, tropical), leaf
106 phenology (broadleaf versus evergreen) and photosynthetic pathway (C_3 versus C_4). The vegetation distribution in
107 each grid cell is prescribed using yearly-varying PFT maps, derived from the ESA Climate Change Initiative (CCI)
108 land cover products (Poulter et al., 2015).

109 Soil parameters such as soil porosity, wilting point, and field capacity are derived from a global map of soil textures
110 based on the FAO/USDA (Food and Agriculture Organization of the United Nations/United States Department of
111 Agriculture) texture classification with 12 texture classes (Reynolds et al., 2000). The different textures for the
112 USDA classification are presented in Table S1 in the supporting information. To better represent the observed soil
113 conditions at the different sites, we substituted the soil textures initially assigned in ORCHIDEE from the USDA
114 texture global map with the observed soil textures corresponding to the USDA texture classes (Table S2). In a
115 previous study of vegetation COS fluxes in ORCHIDEE, Maignan et al. (2021) used the global soil map based on
116 the Zobler texture classification (Zobler, 1986), which is reduced to 3 different textures in ORCHIDEE. However,
117 the USDA soil classification gives a finer description of the different soil textures than the Zobler soil
118 classification, considering 12 soil textures instead of 3. The move from the coarse Zobler classes to the finer USDA
119 classes is found to be more important to the mechanistic model. Since the USDA texture classes are more accurate
120 with its finer discretization of soil textures, in the rest of this study, we only illustrate the results based on the
121 USDA texture classification.

122



123

124 For site level simulations, the ORCHIDEE LSM was forced by local micro-meteorological measurements obtained
125 from the FLUXNET network at the FLUXNET sites following the Creative Commons (CC-BY 4.0) license
126 (Pastorello et al., 2020), and at the remaining sites by other local meteorological measurements performed together
127 with the COS fluxes measurements when available, eventually gap-filled using the $0.25^\circ \times 0.25^\circ$, hourly reanalysis
128 from the fifth generation of meteorological analyses of the European Centre for Medium-Range Weather Forecasts
129 (ECMWF) (ERA5) (Hersbach et al., 2020). Global simulations were forced by the 0.5° and 6-hourly CRUJRA
130 reanalysis (Friedlingstein et al., 2020). Near-surface COS concentrations (noted C_a below) were prescribed using
131 monthly-mean atmospheric COS concentrations at the first vertical level of the LMDZ atmospheric transport
132 model (GCM, see description below in Sect. 2.1.3), forced with optimized COS surfaces fluxes. The latter have
133 been inferred by atmospheric inverse modelling from the COS surface measurements of the NOAA network
134 (Remaud et al., 2021). Simulations with constant atmospheric COS concentrations at a mean global value of 500
135 ppt were also run, to evaluate the impact of spatio-temporal variations of near-surface COS concentrations versus
136 a constant value. Near-surface CO_2 concentrations were estimated using global yearly-mean values provided by
137 the TRENDY project (Sitch et al., 2015).

138 2.1.2 COS soil models

139 The empirical soil COS flux model

140 We implemented in the ORCHIDEE LSM the soil COS flux model from Berry et al. (2013), which assumes that
141 COS uptake is proportional to CO_2 production by soil respiration, following Yi et al. (2007). Although Yi et al.
142 (2007) reported a relationship between soil COS uptake and total soil respiration, including root respiration, Berry
143 et al. (2013) assumed that COS flux was proportional to soil heterotrophic respiration only. The rationale behind
144 this assumption is that soil CA concentration is related to soil organic matter content, and thus ecosystem
145 productivity (Berry et al., 2013). As heterotrophic respiration is also linked to productivity, Berry et al. (2013)
146 considered soil COS uptake to be proportional to soil heterotrophic respiration. However, soil respiration alone
147 did not correlate well in incubation studies (Whelan et al., 2016). As the proportionality between COS fluxes and
148 soil respiration has only been demonstrated for the total (heterotrophic and autotrophic) soil respiration (Yi et al.
149 2007), we used in this study total soil respiration as a scaling factor for soil COS uptake. This model will be
150 referred to as the empirical model.

151

152 The influence of soil temperature and moisture are included in the calculation of soil respiration. Thus, we
153 computed soil COS flux $F_{\text{soil,empirical}}$ ($\text{pmol COS m}^{-2} \text{ s}^{-1}$) as follows,

$$154 F_{\text{soil,empirical}} = -k_{\text{soil}} * \text{Resp}_{\text{tot}} \quad (1)$$

155 where Resp_{tot} is total soil respiration ($\mu\text{mol CO}_2 \text{ m}^{-2} \text{ s}^{-1}$) and k_{soil} is a constant equal to $1.2 \text{ pmol COS } \mu\text{mol}^{-1}$
156 CO_2 that converts CO_2 production from respiration to COS uptake. The value of $1.2 \text{ pmol COS } \mu\text{mol}^{-1}$ was
157 estimated from field chamber measurements in a pine and broadleaf mixed forest (Dinghushan Biosphere Reserve,
158 south China) from Yi et al. (2007). In ORCHIDEE, we calculated the total soil respiration as the sum of soil
159 heterotrophic respiration within the soil column, including that of the litter, and root autotrophic respiration.



160 **The mechanistic soil COS flux model**

161 The mechanistic COS soil model of Ogée et al. (2016) describes both soil COS uptake and production. This model
162 includes COS diffusion in the soil matrix, COS dissolution and hydrolysis in the water-filled pore space and COS
163 production under low redox conditions. COS advection is neglected as the advective flux becomes negligible for
164 time scales longer than 1 h (Ogée et al., 2016). The soil is assumed to be horizontally homogeneous so that the
165 soil COS concentration C (mol m^{-3}) is only a function of time t (s) and soil depth z (m). The mass balance equation
166 for COS can then be written as (Ogée et al., 2016),

$$167 \quad \frac{\partial \varepsilon_{tot} C}{\partial t} = - \frac{\partial F_{diff}}{\partial z} + P - S \quad (2)$$

168 with ε_{tot} the soil total porosity (m^3 air m^{-3} soil), F_{diff} the diffusional flux of COS ($\text{mol m}^{-2} \text{s}^{-1}$), S the COS
169 consumption rate ($\text{mol m}^{-3} \text{s}^{-1}$) and P the COS production rate under low redox conditions ($\text{mol m}^{-3} \text{s}^{-1}$).

170 Under steady-state conditions and uniform soil temperature, moisture and porosity profiles, an analytical solution
171 of Eq. 2 can be found (Ogée et al., 2016). Although Eq. 2 could also be solved numerically using the soil
172 discretization in ORCHIDEE, we preferred to use the analytical solution, using the mean soil moisture and
173 temperature averaged over the first few soil layers (down to about 9 cm deep), weighted by the thickness of each
174 soil layer. Assuming fully mixed atmospheric conditions within and below the vegetated canopy, we also assumed
175 that the COS concentration at the soil surface $C(z=0)$ is equal to the near-surface COS concentration C_a . With
176 these boundaries' conditions, the steady-state COS flux at the soil surface $F_{soil,mechanistic}$ ($\text{mol m}^{-2} \text{s}^{-1}$) is (Ogée
177 et al., 2016),

$$178 \quad F_{soil,mechanistic} = \sqrt{kB\theta D} \left(C_a - \frac{z_1^2 P}{D} (1 - \exp(-z_{max}/z_1)) \right) \quad (3)$$

179 with k the first-order COS consumption rate constant within the soil (s^{-1}), B the solubility of COS in water (m^3
180 water m^{-3} air), θ the soil volumetric water content (m^3 water m^{-3} soil), D the total effective COS diffusivity (m^2
181 s^{-1}), $z_1 = \sqrt{D/kB\theta}$ (m) and z_{max} the soil depth below which the COS production rate and the soil COS gradient
182 are assumed negligible (Ogée et al., 2016). In the following, z_{max} is set at 0.09 m.

183 COS diffusion

184 The total effective COS diffusivity in soil, D , includes the effective diffusivity of gaseous COS $D_{eff,a}$ (m^3 air m^{-1}
185 soil s^{-1}) and dissolved COS $D_{eff,l}$ (m^3 water m^{-1} soil s^{-1}) through the soil matrix,

$$186 \quad D = D_{eff,a} + D_{eff,l} B \quad (4)$$

187 The solubility of COS in water B is calculated using Henry's law constant K_H ($\text{mol m}^{-3} \text{Pa}^{-1}$),

$$188 \quad B = K_H R T \quad (5)$$

189 with $R = 8,314 \text{ J mol}^{-1} \text{K}^{-1}$ the ideal gas constant and T the soil temperature (K) and (Wilhelm et al., 1977),

$$190 \quad K_H = 0.00021 \exp[24900/R(1/T - 1/298,15)] \quad (6)$$



191 The effective diffusivity of gaseous COS $D_{eff,a}$ is expressed as (Ogée et al., 2016),

$$192 \quad D_{eff,a} = D_{0,a} \tau_a \varepsilon_a \quad (7)$$

193 with $D_{0,a}$ the binary diffusivity of COS in the air ($\text{m}^2 \text{air s}^{-1}$), τ_a the air tortuosity factor representing the tortuosity
194 of the air-filled pores, and ε_a is the air-filled porosity ($\text{m}^3 \text{air m}^{-3} \text{soil}$). The binary diffusivity of COS in the air
195 $D_{0,a}$ is expressed following the Chapman-Enskog theory for ideal gases (Bird et al., 2002) and depends on
196 temperature and pressure,

$$197 \quad D_{0,a}(T, p) = D_{0,a}(T_0, p_0) \left(\frac{T}{T_0}\right)^{1.5} \left(\frac{p}{p_0}\right) \quad (8)$$

198 with $D_{0,a}(T_0, p_0) = D_{0,a}(25^\circ\text{C}, 1 \text{ atm}) = 1.27 \times 10^{-5} \text{ m}^2 \text{ s}^{-1}$ (Massman, 1998).

199 The expression of the air tortuosity factor τ_a depends on whether the soil is repacked or undisturbed. In
200 ORCHIDEE, repacked soils correspond to the agricultural soils represented by the C₃ and C₄ crops. Soils not
201 covered by crops are considered as undisturbed soils. The expression of τ_a for repacked soils $\tau_{a,r}$ is given by
202 Moldrup et al. (2003),

$$203 \quad \tau_{a,r} = \varepsilon_a^{3/2} / \varphi \quad (9)$$

204 with φ the soil porosity ($\text{m}^3 \text{m}^{-3}$) that includes the air-filled and water-filled pores. Soil porosity is assumed constant
205 through the soil column in ORCHIDEE and is determined by the USDA texture global map. The air-filled porosity
206 ε_a is calculated as $\varepsilon_a = \varphi - \theta$.

207 The expression of τ_a for undisturbed soils $\tau_{a,u}$ is given in Deepagoda et al. (2011). We chose this expression rather
208 than the expression proposed by Moldrup et al. (2003) for undisturbed soils because it appears to be more accurate
209 and does not require information on the pore-size distribution (Ogée et al., 2016),

$$210 \quad \tau_{a,u} = [0.2(\varepsilon_a/\varphi)^2 + 0.004] / \varphi \quad (10)$$

211 In a similar way to COS diffusion in the gas phase, the effective diffusivity of dissolved COS $D_{eff,l}$ is described
212 by Ogée et al. (2016),

$$213 \quad D_{eff,l} = D_{0,l} \tau_l \theta \quad (11)$$

214 with $D_{0,l}$ the binary diffusivity of COS in the free water ($\text{m}^2 \text{water s}^{-1}$) and τ_l the tortuosity factor for solute
215 diffusion. The binary diffusivity of COS in the free water $D_{0,l}$ is described using an empirical formulation proposed
216 by Zeebe (2011) for CO₂, which only depends on temperature,

$$217 \quad D_{0,l}(T) = D_{0,l}(T_0) \left(\frac{T}{T_0} - 1\right)^2 \quad (12)$$

218 with $T_0 = 216\text{K}$ (Ogée et al., 2016) and $D_{0,l}(25^\circ\text{C}) = 1.94 \times 10^{-9} \text{ m}^2 \text{ s}^{-1}$ (Ulshöfer et al., 1996).

219 The expression of τ_l is the same for repacked and undisturbed soils. We used the expression given by Millington
220 and Quirk (1961) as a good compromise between simplicity and accuracy (Moldrup et al. 2003),



221 $\tau_l = \theta^{7/3} / \varphi^2$ (13)

222 COS consumption

223 COS can be destroyed by biotic and abiotic processes. The abiotic process corresponds to COS hydrolysis in soil
224 water at an uncatalyzed rate k_{uncat} (s^{-1}), which depends on soil temperature T (K) and pH (Elliott et al., 1989),

225 $k_{\text{uncat}} = 2.15 \cdot 10^{-5} \exp\left(-10450\left(\frac{1}{T} - \frac{1}{298.15}\right)\right) + 12.7 \cdot 10^{-pK_w + pH} \exp\left(-6040\left(\frac{1}{T} - \frac{1}{298.15}\right)\right)$ (14)

226 with pK_w the dissociation constant of water.

227 This uncatalyzed hydrolysis is quite low compared to the COS hydrolysis catalysed by soil microorganisms, which
228 is the main contribution of COS uptake by soils (Kesselmeier et al., 1999; Sauze et al., 2017; Meredith et al.,
229 2018). The enzymatic reaction catalysed by CA follows Michaelis-Menten kinetics. The turnover rate k_{cat} (s^{-1})
230 and the Michaelis-Menten constant K_m (mol m^{-3}) of this reaction depend on temperature. The temperature
231 dependence of the ratio $\frac{k_{\text{cat}}}{K_m}$ is expressed as (Ogée et al., 2016),

232 $x_{CA}(T) = \frac{\exp\left(-\frac{\Delta H_a}{RT}\right)}{1 + \exp\left(-\frac{\Delta H_d + \Delta S_d}{RT} + \frac{\Delta S_d}{R}\right)}$ (15)

233 where ΔH_a , ΔH_d and ΔS_d are thermodynamic parameters, such as $\Delta H_a = 40 \text{ kJ mol}^{-1}$, $\Delta H_d = 200 \text{ kJ mol}^{-1}$ and ΔS_d
234 $= 660 \text{ J mol}^{-1} \text{ K}^{-1}$.

235 The total COS consumption rate by soil k (s^{-1}) is described with respect to the uncatalyzed rate at $T = 298.15 \text{ K}$
236 and $pH = 4.5$ (Ogée et al., 2016),

237 $k = f_{CA} k_{\text{uncat}}(298.15, 4.5) \frac{x_{CA}(T)}{x_{CA}(298.15)}$ (16)

238 where f_{CA} is the CA enhancement factor, which characterizes the soil microbial community that can consume
239 COS. The CA enhancement factor depends on soil CA concentration, temperature, and pH. Ogée et al. (2016)
240 reported that its values range between 21 600 and 336 000, with a median value at 66 000. We adapted the values
241 of f_{CA} found in (Meredith et al., 2019) to have a CA enhancement factor that depends on ORCHIDEE biomes
242 (Appendix A, Table A1).

243 Oxic soil COS production

244 Abiotic oxic soil COS production has been observed at high soil temperature (Maseyk et al., 2014; Whelan and
245 Rhew, 2015; Kitz et al., 2017, 2020; Spielmann et al., 2019, 2020). However, photodegradation has also been
246 proposed as an abiotic production mechanism in oxic soils (Whelan and Rhew, 2015; Kitz et al., 2017, 2020).
247 Abiotic COS production is still not well understood but was assumed to originate from biotic precursors (Meredith
248 et al., 2018).

249 In Ogée et al. (2016), the production rate P is described as independent of soil pH but depends on soil temperature
250 and redox potential. This dependence on soil redox potential enables us to consider the transition between oxic
251 and anoxic soils. However, because little information is available on soil redox potential at the global scale, its
252 influence cannot yet be represented in a spatially and temporally dynamic way in a land surface model such as



253 ORCHIDEE. Thus, we decided to use the production rate described in Whelan et al. (2016) that only depends on
 254 soil temperature and land use type,

$$255 \quad P_{oxic} = e^{\alpha + \beta T} \quad (17)$$

256 where P_{oxic} is expressed in $\text{pmol g}^{-1} \text{min}^{-1}$, T is soil temperature ($^{\circ}\text{C}$) and α and β are parameters determined by
 257 Whelan et al. (2016) for each land use type using the least-squares fitting approach. We adapted the values of α
 258 and β given for four land use types to ORCHIDEE biomes (Appendix A Table A2). Values of α and β for deserts
 259 could not be estimated by Whelan et al. (2016) because COS emission for this biome was not found to increase
 260 with temperature. Figure 11 in Whelan et al. (2016) shows that COS emission from a desert soil is always near
 261 zero for temperatures ranging from 10°C to 40°C . Moreover, COS emission from a desert soil is also found to be
 262 near zero in Fig. 1 of Meredith et al. (2018). This could be explained by a lack of organic precursors to produce
 263 COS (Whelan et al., 2016). Therefore, we considered that desert soils, which correspond to a specific non-
 264 vegetated PFT in ORCHIDEE, do not emit COS. For other ORCHIDEE biomes, COS production was estimated
 265 using α and β for each PFT and the mean soil temperature over the top 9 cm. The unit of P_{oxic} was converted from
 266 $\text{pmol g}^{-1} \text{min}^{-1}$ to $\text{mol m}^{-3} \text{s}^{-1}$ (in equation 3) using soil bulk density information from the Harmonized World Soil
 267 Database (HWSD; FAO/IIASA/ISRIC/ISSCAS/JRC, 2012).

268

269 Anoxic soil COS production

270 Several studies have shown direct COS emissions by anoxic soils (Devai and DeLaune, 1997; de Mello and Hines,
 271 1994; Whelan et al., 2013; Yi et al., 2007). This has been linked to a strong activity of sulfate reduction
 272 metabolisms in highly reduced environments such as wetlands (Aneja et al., 1981; Kanda et al., 1992; Whelan et
 273 al., 2013; Yi et al., 2007). A previous approach developed by Launois et al. (2015) was based on the representation
 274 of seasonal methane emissions by Wania et al. (2010) in the LPJ-WHyME model to represent anoxic soils in
 275 ORCHIDEE. The mean values of soil COS emissions from Whelan et al. (2013) were used to attribute to each
 276 grid point a value of soil COS emission. In this approach by Launois et al. (2015), salt marshes were not represented
 277 despite their strong COS emissions found in Whelan et al. (2013). Emissions from rice paddies were also neglected.
 278 Thus, COS emissions from anoxic soils peaked in summer over the high latitudes, following methane production.
 279 Because of the scarce knowledge on anoxic soil COS exchange, here we propose another approach to represent
 280 the contribution of anoxic soils, which could be compared to the previous approach developed by Launois et al.
 281 (2015). To represent the distribution of anoxic soils we selected the regularly flooded wetlands from the map
 282 developed by Tootchi et al. (2019), as represented in Fig. 1. The regularly flooded wetlands cover 9.7% of the
 283 global land area, which is among the average values found in the literature ranging from 3% to 21% (Tootchi et
 284 al., 2019). The pixels defined as anoxic soils are considered flooded through the entire year: the seasonal variations
 285 of the flooding, as happening during the monsoon seasons, are consequently neglected.

286 The production rate for anoxic soils is based on the expression developed by Ogée et al. (2016),

$$287 \quad P_{anoxic} = P_{ref} z_{max} Q_{10}^{\frac{(T - T_{ref})}{10}} \quad (18)$$



288 with P_{ref} ($\text{mol m}^{-2} \text{s}^{-2}$) the reference production term, T_{ref} a reference soil temperature (K) and Q_{10} the
289 multiplicative factor of the production rate for a 10°C increase in soil temperature (unitless). As anoxic soil
290 production ranges from 10 to $300 \text{ pmol m}^{-2} \text{s}^{-1}$ for salt marshes and is usually below $10 \text{ pmol m}^{-2} \text{s}^{-1}$ for freshwater
291 wetlands (Whelan et al., 2018), the reference production term was set to $10 \text{ pmol m}^{-2} \text{s}^{-1}$.

292 All the variables and constants of the empirical and mechanistic models are presented in Appendix A Tables A3
293 and A4.

294 **2.1.3 The atmospheric chemistry transport model LMDZ**

295 To simulate the COS atmospheric distribution, we use an “offline” version of the Laboratoire de Météorologie
296 Dynamique General Circulation Model (GCM), LMDZ 6 (Hourdin et al., 2020), which has been used as the
297 atmospheric component in the IPSL Coupled Model for CMIP6. The LMDZ GCM has a spatial resolution
298 $3.75^\circ\text{long} \times 1.9^\circ\text{lat}$. with 39 sigma-pressure layers extending from the surface to about 75 km, corresponding to a
299 vertical resolution of about 200-300 m in the planetary boundary layer, and a first level at 33 m above sea or
300 ground level. The model u and v wind components were nudged towards winds from ERA5 reanalysis with a
301 relaxation time of 2.5 hours to ensure realistic wind advection (Hourdin and Issartel, 2000; Hauglustaine et al.,
302 2004). The ECMWF fields are provided every 6 hours and interpolated onto the LMDZ grid. This version has
303 been shown to reasonably represent the transport of passive tracers (Remaud et al., 2018). The off-line model uses
304 pre-computed mass-fluxes provided by this full LMDZ GCM version and only solves the continuity equation for
305 the tracers, which significantly reduces the computation time. In the following, we refer to this offline version as
306 LMDZ. The model time step is 30 minutes, and the output concentrations are 3-hourly averages.

307 The atmospheric COS oxidation is computed from pre-calculated OH monthly concentration fields produced from
308 a simulation of the INCA (Interaction with Chemistry and Aerosols) model (Folberth et al., 2006; Hauglustaine et
309 al., 2004, 2014) coupled to LMDZ. The atmospheric OH oxidation of COS amounts to 100 GgS yr^{-1} in the model.
310 Similarly, the COS photolysis rates are also pre-calculated with the INCA model, which uses the Troposphere
311 Ultraviolet and Visible (TUV) radiation model (Madronich et al., 2003) adapted for the stratosphere (Terrenoire
312 et al., in prep.). The temperature-dependent carbonyl sulfide absorption cross-sections from 186.1 nm to 296.3 nm
313 are taken from (Burkholder et al., 2019). The calculated photolysis rates are averaged over the period 2008-2018
314 and prescribed to LMDZ. Implemented in LMDZ, the COS photolysis in the stratosphere amounts to about 30
315 GgS yr^{-1} , which of the same order of magnitude as previous estimates: 21 GgS yr^{-1} (71% of 30 GgS yr^{-1}) by Chin
316 and Davis (1995), between 11 GgS yr^{-1} and 21 GgS yr^{-1} by Kettle et al. (2002) and between 16 GgS yr^{-1} and 40
317 GgS yr^{-1} by Ma et al. (2021).

318 **2.2 Observation data sets**

319 **2.2.1 Description of the sites**

320 The description of the studied sites is given in Table 1.

321 **2.2.2 Soil COS flux determination at selected sites**

322 Soil COS flux chamber measurements were conducted in 2015 at AT-NEU, in 2016 at DK-SOR, ES-LMA and
323 ET-JA, and in 2017 at IT-CRO (abbreviations as in Table 1). The aboveground vegetation was removed one day
324 before the measurements if needed and the fluxes were derived from concentration measurements using a Quantum



325 Cascade Laser (see Kitz et al., 2020 and Spielmann et al., 2020, 2019). At AT-NEU, DK-SOR, ES-LMA and IT-
326 CRO, a Random Forest model was calibrated against the manual chamber measurements, and then used to simulate
327 half-hourly soil COS fluxes in Spielmann et al. (2019). We compared the ORCHIDEE half-hourly simulated fluxes
328 to half-hourly outputs of the Random Forest model. This enabled to study the diel cycle, and to compute daily
329 observations with no sampling bias for the study of the seasonal cycle. Soil COS fluxes for ET-JA were derived
330 by using the same training method than the one used in Spielmann et al. (2019).

331 At FI-HYY, soil COS fluxes were measured using two automated soil chambers in 2015. These chambers were
332 connected to a quantum cascade laser spectrometer to calculate soil COS fluxes from concentration measurements
333 (see Sun et al. (2018) for more information on the experimental setup).

334 At US-HA, soil COS fluxes were not directly measured but derived from eddy covariance COS and CO₂
335 measurements and soil chamber CO₂ measurements conducted in 2012 and 2013. A sub-canopy flux gradient
336 approach was used to partition canopy uptake from soil COS fluxes. For more information on this approach and
337 its limitations, see Wehr et al. (2017).

338 In the study of soil COS fluxes, the difficulty of performing soil COS flux measurements must be acknowledged,
339 as well as the differences between experimental setups and methods to retrieve soil COS fluxes. These limitations
340 are illustrated in the set of observations selected here. Aboveground vegetation had to be removed at some sites to
341 not measure the plant contribution in addition to soil COS fluxes (Sun et al., 2018; Spielmann et al., 2019; Kitz et
342 al., 2020). Vegetation removal prior to the measurements might lead to artefacts in the observations. Some
343 components of the measuring system can also emit COS. In this case, a blank system is needed to apply a post-
344 correction to the measured fluxes (Sun et al., 2018; Kitz et al., 2020). Litter was left in place at the measurement
345 sites.

346 **2.2.3 COS concentrations at the NOAA/ESRL sites**

347 The NOAA surface flask network provides long-term measurements of the COS mole fraction at 14 locations at
348 weekly to monthly frequencies from the year 2000 onwards. We use an extension of the data initially published in
349 Montzka et al. (2007). The data were collected as paired flasks analyzed using gas chromatography and mass
350 spectrometry. The stations located in the northern Hemisphere sample air masses coming from the entire northern
351 hemisphere domain above 30 degrees. Among them, the sites LEF, NWR, HFM, WIS have a mostly continental
352 footprints (Remaud et al., 2021) while the sites SPO, CGO, PSA sample mainly oceanic air masses of the southern
353 hemisphere (Montzka et al., 2007). The locations of these sites are depicted in Appendix B, Fig. B1.

354 **2.3 Simulations**

355 **2.3.1 Spin-up phase**

356 A “spin-up” phase was performed before each simulation, which enabled all carbon pools to stabilize and the net
357 biome production to oscillate around zero. Reaching the equilibrium state is accelerated in the ORCHIDEE LSM
358 thanks to a pseudo-analytical iterative estimation of the carbon pools, as described in Lardy et al. (2011). For site
359 simulations, the spin-up was performed by cycling the years available in the forcing files of each site, for a total
360 of about 340 years. For global simulations, the spin-up phase of 340 years was performed by cycling over 10 years
361 of meteorological forcing files in the absence of any disturbances.



362 **2.3.2 Transient phase**

363 Following the spin-up phase we ran a transient simulation of about 40 years that introduced disturbances such as
364 climate change, land use change and increasing CO₂ atmospheric concentrations.

365 This transient phase was performed by cycling over the available years for site simulations. For global simulations,
366 the transient phase was run where we introduced disturbances from 1860 to 1900. After this transient phase, COS
367 fluxes were simulated from 1901 to 2019.

368 **2.3.3 Atmospheric simulations: sampling and data processing**

369 We ran the LMDZ6 version of the atmospheric transport model described above for the years 2009 to 2016. We
370 started from a uniform initial condition and we remove the first year as it is considered to be part of the spin-up
371 period. The prescribed COS fluxes used as model inputs are presented in Table 2. The fluxes are given as a lower
372 boundary condition, called the surface, of the atmospheric transport model (LMDZ), which then simulates the
373 transport of COS by large-scale advection and sub-grid scale processes such as convection and boundary layer
374 turbulence. In this study, we only evaluate the sensitivity of the latitudinal gradient and seasonal cycle of COS
375 concentrations to the soil COS fluxes. The horizontal gradient aims at validating the latitudinal repartition of the
376 surface fluxes, while the seasonal cycle partly reflects the seasonal exchange with the terrestrial sink, which peaks
377 in spring/summer. This study does not aim at reproducing the mean value as the top-down COS budget is currently
378 unbalanced, with a source component missing (Whelan et al., 2018; Remaud et al., 2021, and see Table 5).

379 For each COS observation, the 3D simulated concentration fields were sampled at the nearest grid point to the
380 station and at the closest hour of the measurements. For each station, the curve fitting procedure developed by the
381 NOAA Climate Monitoring and Diagnostic Laboratory (NOAA/CMDL) (Thoning et al., 1989) was applied to
382 modelled and observed COS time series to extract a smooth detrended seasonal cycle. We first fitted a function
383 including a first-order polynomial term for the growth rate and two harmonic terms for seasonal variations. The
384 residuals (raw time series minus the smooth curve) were fitted using a lowpass filter with either 80 or 667 d as
385 short-term and long-term cut-off values. The detrended seasonal cycle is defined as the smooth curve (full function
386 plus short-term residuals) minus the trend curve (polynomial plus long-term residuals). Regarding vegetation COS
387 fluxes (Maignan et al., 2021), we added the possibility to use spatially and temporally varying atmospheric COS
388 concentrations, as for soil.

389 **2.4 Numerical methods for model evaluation and parameter optimisation**

390 **2.4.1 Statistical scores**

391 We evaluated modelled soil COS fluxes against field measurements using the Root Mean Square Deviation
392 (RMSD):

393
$$RMSD = \sqrt{\frac{\sum_{n=1}^N (F_{COS}^{Obs}(n) - F_{COS}^{Mod}(n))^2}{N}}$$
 (19)

394 where N is the number of considered observations, $F_{COS}^{Obs}(n)$ is the n th observed COS flux and $F_{COS}^{Mod}(n)$ is the n th
395 modelled COS flux, and the relative RMSD (rRMSD):



$$396 \quad rRMSD = \frac{RMSD}{\frac{\sum_{n=1}^N r_{COS}^{Obs}(n)}{N}} \quad (20)$$

397 which is the RMSD divided by the mean value of observations.

398 Simulated atmospheric COS concentrations were evaluated by computing the normalized standard deviations
399 (NSDs), which is the standard deviation of the simulated concentrations divided by the mean of the observed
400 concentrations, and the Pearson correlation coefficients (r) between simulated and observed COS concentrations.
401 The closer NSD and r values are to 1, the better the model accuracy is.

402 2.4.2 Data assimilation

403 One of the main difficulties with the implementation of a model is to define the parameter values that lead to the
404 most accurate representation of the processes in ORCHIDEE. Calibrating the model parameters is of interest as
405 Ogée et al. (2016) indicate that some of the model parameters such as f_{CA} and the production term parameters have
406 to be constrained by observations. Moreover, the default values for the soil COS model parameters used in this
407 study (Appendix A Tables A1 and A2) are determined by laboratory experiments (Ogée et al., 2016; Whelan et
408 al., 2016), that is why it is interesting to study how the values obtained by calibration against field observations
409 differ from these default values. Data assimilation (DA) aims at producing an optimal estimate by combining
410 observations and model outputs. In this study, we used data assimilation to find the model parameter values that
411 improve the fit between simulated and observed soil COS fluxes from the empirical and the mechanistic models.
412 We used the ORCHIDEE DA System (ORCHIDAS), which is based on a Bayesian framework. ORCHIDAS has
413 been described in detail in previous studies (Bastrikov et al., 2018; Kuppel et al., 2014; MacBean et al., 2018;
414 Peylin et al., 2016; Raoult et al., 2021), so below we only briefly present the method. Assuming that the
415 observations and model outputs follow a Gaussian distribution, we aim at minimizing the following cost function
416 $J(x)$ by optimizing the model parameters (Tarantola, 2005),

$$417 \quad J(x) = \frac{1}{2} [(M(x) - y)^T \cdot E^{-1} \cdot (M(x) - y) + (x + x^b)^T \cdot B^{-1} \cdot (x + x^b)] \quad (21)$$

418 with x the vector of parameters to optimize and y the observations. The first part of the cost function measures the
419 mismatch between the observations and the model, and the second part represents the mismatch between the prior
420 parameter values x^b and the considered set of parameters x . Both terms of the cost function are weighted by the
421 prior covariance matrices for the observation errors E^{-1} and parameter errors B^{-1} . The minimization of the cost
422 function follows the genetic algorithm (GA) method, which is derived from the principles of genetics and natural
423 selection (Goldberg, 1989; Haupt and Haupt, 2004) and is described for ORCHIDAS in Bastrikov et al. (2018).
424 For each soil COS model, we selected the 8 most important parameters to which soil COS fluxes are sensitive
425 following sensitivity analyses (Sect. 2.4.3). The observation sites selected for sensitivity analyses and DA are the
426 ones with the largest number of observations for model parameter calibration, which are FI-HYY and US-HA.

427 2.4.3 Sensitivity analyses

428 We conducted sensitivity analyses at two contrasting sites (FI-HYY and US-HA) to determine which model
429 parameters have the most influence on the simulated soil COS fluxes from the empirical and the mechanistic
430 models. Sensitivity analyses can help to identify the key parameters before aiming at calibrating these parameters.



431 Indeed, focusing on the key model parameters for calibration limits both the computational cost of optimization
432 that increases with the number of parameters and the risk of overfitting.

433 The Morris method (Morris, 1991; Campolongo et al., 2007) was used for the sensitivity analysis as it is relatively
434 time-efficient and enables ranking the parameters by importance. This qualitative method requires only a small
435 number of simulations, $(p+1)n$, with p the number of parameters and n the number of random trajectories generated
436 (here, $n=10$).

437 We selected a set of parameters for the Morris sensitivity analyses based on previous sensitivity analyses conducted
438 on soil parameters in ORCHIDEE (Dantec-Nédélec et al., 2017; Raoult et al., 2021; Mahmud et al., 2021). A
439 distinction is made between the soil COS model parameters called first-order parameters (f_{CA} , α and β for the
440 mechanistic model and k_{soil} for the empirical model), and parameters called second-order parameters related to
441 soil hydrology, carbon uptake and allocation, phenology, conductance, or photosynthesis (18 parameters, see
442 Tables S3 and S4). The range of variation of the second-order parameters are described in previous studies using
443 ORCHIDEE (Dantec-Nédélec et al., 2017; Raoult et al., 2021; Mahmud et al., 2021). For the first-order
444 parameters, the range of variation is described in Yi et al. (2007) for k_{soil} (± 1.08 pmol COS μmol^{-1} CO₂) and in
445 Table 1 in Meredith et al. (2019) for f_{CA} . The ranges of variation for α and β parameters are not directly given in
446 the literature and were calculated based on information from the production parameters defined in Meredith et al.
447 (2018) (Text S1 and Table S5).

448 3 Results

449 3.1 Site scale COS fluxes

450 3.1.1 Soil COS flux seasonal cycles

451 Figure 2 shows the seasonal cycles of soil COS fluxes at the different sites where measurements were conducted.
452 The empirical model mainly differs from the mechanistic model with a stronger seasonal amplitude of soil COS
453 fluxes (34% higher), except at the sites where a net COS production is found with the mechanistic model in summer
454 (ES-LMA and IT-CRO). At all sites, the empirical model shows that the simulated uptake increases in spring
455 reaching a maximum in summer, and decreases in autumn with a minimal uptake during winter. The strong COS
456 uptake in summer from the empirical model can be explained by the proportionality of soil COS uptake to
457 simulated soil respiration, which increases with the high temperatures in summer. In contrast, the mechanistic
458 model depicts almost no seasonality at all the sites where no net COS production is found over the year. As the
459 mechanistic model represents both soil COS uptake and production, the increase in COS production due to higher
460 temperature in summer compensates part of the COS uptake (Appendix C Figure C1). While the uptake from the
461 empirical model is often higher than the one computed with the mechanistic model in summer, soil COS uptake
462 in winter is stronger with the mechanistic representation.

463 The scarcity of field measurements at AT-NEU, ES-LMA, IT-CRO, DK-SOR and ET-JA does not allow an
464 evaluation of the simulated seasonality of COS fluxes. However, at US-HA, the absence of seasonality from May
465 to October in the observations is also found in the mechanistic model, while a maximum net soil COS uptake is
466 reached with the empirical model.

467 We found that the mechanistic model is in better agreement with the observations for 4 (IT-CRO, ET-JA, FI-HYY,
468 US-HA) out of the 7 sites (Table 3), with a mean of 1.58 pmol $\text{m}^{-2} \text{s}^{-1}$ and 2.03 $\text{m}^{-2} \text{s}^{-1}$ for the mechanistic and
469 empirical model, respectively. However, the mechanistic model struggles to reproduce soil COS fluxes at AT-



470 NEU and ES-LMA, with an overestimation of soil COS uptake or an underestimation of soil COS production at
471 AT-NEU and a delay in the simulated net COS production at ES-LMA. We might suspect that the removal of
472 vegetation at these sites prior to the measurements could have artificially enhanced COS production in the
473 observations. The mechanistic model is able to represent a net COS production at IT-CRO but overestimates it.
474 This might highlight the importance of adapting the production parameters (α and β) in this model to adequately
475 represent a net COS production. As expected, the empirical model is unable to correctly simulate the direction of
476 the observed positive soil COS exchange rates at ES-LMA and IT-CRO.

477 3.1.2 Soil COS flux diel cycles

478 Figure 3 shows the comparison between the simulated and observed mean diel cycles over a month. The
479 observations show a minimum net soil COS uptake or a maximum net soil COS production reached between 11
480 am and 1 pm at AT-NEU, ES-LMA, IT-CRO and DK-SOR. A minimum net soil COS uptake is also observed at
481 US-HA but in the afternoon. At AT-NEU and ES-LMA, neither model is able to represent the observed diel cycle.
482 At IT-CRO, DK-SOR and US-HA, the diel cycles simulated by the mechanistic model show patterns similar to
483 the observations with a peak in the middle of the day, but with an overestimation of the net soil COS production
484 and a delay in the peak at IT-CRO, and an overestimation of the net soil COS uptake at DK-SOR. The mechanistic
485 model reproduces the absence of a diel cycle observed at FI-HYY. Small diel variations are observed at ET-JA,
486 which are also captured by the mechanistic model but with an underestimation of the net soil COS uptake. As the
487 mechanistic model includes PFT-specific parameters (f_{CA} , α , β), we can think that these parameters would need
488 to be calibrated to improve the model performance at the site-scale. The empirical model shows a maximum soil
489 COS uptake around 3 pm at ET-JA, FI-HYY, US-HA and IT-CRO, which is not found in the observations at FI-
490 HYY and is in contradiction with the observed diel variations at IT-CRO and ES-LMA. Considering all sites, the
491 mechanistic model leads to a smaller error between the simulations and the observations, with a mean RMSD of
492 $1.38 \text{ pmol m}^2 \text{ s}^{-1}$ against $1.87 \text{ pmol m}^2 \text{ s}^{-1}$ for the empirical model (Table 4).

493 3.1.3 Dependency on environmental variables

494 Figure 4 represents simulated net soil COS fluxes versus soil temperature and soil water content at the different
495 sites. At the sites where only a net soil COS uptake is simulated by the mechanistic model (all sites except IT-
496 CRO and ES-LMA), soil COS uptake globally decreases with increasing soil water content, which appears to be
497 the main driver of soil COS fluxes. This behaviour can be explained by a decrease in COS diffusivity through the
498 soil matrix with increasing soil moisture, reducing soil COS availability for microorganism consumption.
499 Furthermore, an optimum soil water content for net soil COS uptake is found between 10% and 15%. This optimum
500 soil moisture is also represented in Ogée et al. (2016) and was described in several field studies to be around 12%
501 (Kesselmeier et al., 1999; Liu et al., 2010; van Diest and Kesselmeier, 2008). The optimum soil water content for
502 soil COS uptake is related to a site-specific temperature optimum, which is found between 13°C and 15°C at US-
503 HA for example. Similarly, a temperature optimum was described in Ogée et al. (2016) and in empirical studies
504 with an optimum value that also depends on the studied site (Kesselmeier et al., 1999; Liu et al., 2010; van Diest
505 and Kesselmeier, 2008). At IT-CRO and ES-LMA where a strong net soil COS production is simulated by the
506 mechanistic model, the main driver of soil COS fluxes becomes soil temperature. At these sites, the net soil COS



507 production increases with soil temperature, due to the exponential response of soil COS production term to soil
508 temperature.

509 Contrary to the mechanistic model, soil COS uptake computed with the empirical model is mainly driven by soil
510 temperature, with a soil COS uptake that increases with increasing soil temperature. This response of the empirical
511 model to soil temperature is due to its relation to soil respiration, which is enhanced by strong soil temperature.
512 However, low soil moisture values were found to limit soil COS uptake for the empirical model, as seen at ES-
513 LMA for a soil water content below 8%.

514 3.1.4 Sensitivity analyses of soil COS fluxes to parameterization

515 Sensitivity analyses including a set of parameters (19 for the empirical model and 21 for the mechanistic model)
516 were performed to evaluate the sensitivity of soil COS fluxes to each of the selected parameter. The Morris scores
517 were normalised by highest values to help rank the parameters by their relative influence on soil COS fluxes, a
518 score of 1 represents the most important parameter and 0 represents the parameters that have no influence on soil
519 COS fluxes. For reasons of clarity, in the following we present the results only for the parameters that were found
520 to have an impact on soil COS fluxes (Morris scores not equal to 0).

521

522 Figure 5 shows the results of the Morris sensitivity experiments highlighting the key parameters influencing soil
523 COS fluxes from the empirical and the mechanistic models at FI-HYY and US-HA. For the empirical model at
524 both sites, the first order parameter (k_{soil}) is the most important parameter in the computation of soil COS fluxes,
525 as it directly scales soil respiration to soil COS fluxes. The following parameters to which soil COS fluxes are the
526 most sensitive are the scalar on the active soil C pool content (soilC) and the temperature-dependency factor for
527 heterotrophic respiration (soil_Q10). Indeed, the soilC parameter determines the soil carbon active pool content,
528 which can be consumed by soil microorganisms during respiration, therefore impacting soil COS fluxes from the
529 empirical model. soil_Q10 impacts soil COS fluxes at both sites as it determines the response of soil heterotrophic
530 respiration to temperature, which is included in the proportionality of soil COS fluxes to the total soil respiration
531 in the empirical model. Similarly, one of the second order parameters, the minimum soil wetness to limit the
532 heterotrophic respiration (min_SWC_resp), has an impact on soil COS fluxes from the empirical model only. The
533 importance of min_SWC_resp for soil COS fluxes is found at US-HA but not at FI-HYY. This can be explained
534 by the difference in soil moisture between the two sites, with an annual mean of 16.2% at US-HA and reaching a
535 minimum of only 8.8%, against an annual mean of 17.5% with a minimum of 12.4% at FI-HYY.

536 Contrary to the empirical model, soil COS fluxes computed with the mechanistic model are more sensitive to two
537 second-order parameters, the Van Genuchten water retention curve coefficient n (n) and the saturated volumetric
538 water content (θ_{SAT}). These two second-order parameters are strongly linked to soil hydrology and determine the
539 soil water content, which affects COS diffusion through the soil matrix and its uptake. The Van Genuchten
540 coefficients occur in the relationships linking hydraulic conductivity and diffusivity to soil water content (van
541 Genuchten, 1980). At both sites, the strong impact of the Van Genuchten water retention curve coefficient n on
542 soil COS fluxes simulated with the mechanistic model highlights the critical importance of soil architecture. Thus,
543 soil COS fluxes computed with the mechanistic model are expected to strongly vary according to the different soil
544 types. Then, the first-order parameters (f_{CA} , α and β) also influence soil COS fluxes from the mechanistic model.
545 However, the uptake parameter (f_{CA} of PFT 15, boreal C_3 grass) has the most influence on soil COS fluxes at FI-



546 HYY, while it is the production-related parameter (α of PFT 6, temperate broadleaved summergreen forest) that
547 has the largest impact at US-HA. The stronger influence of the production parameter involved in the temperature
548 response at US-HA might be explained by the difference of temperature between the two sites, which ranges from
549 -10°C to 25°C at US-HA with an annual mean of 7.5°C in 2013, while only ranging from -5°C to 15°C with an
550 annual mean of 4.3°C at FI-HYY in 2015. Similar to the difference in the main driver of soil COS fluxes found in
551 Fig. 4, the most important first-order parameters to which soil COS fluxes are sensitive seem to differ between
552 uptake and production parameters depending on the site conditions. It is to be noted that at US-HA, the most
553 important production parameters are the ones of the dominant PFT at this site (PFT 6), which also correspond to
554 a stronger response of the production term to temperature than for PFT 10 (temperate C_3 grass). However, at FI-
555 HYY the most influential uptake parameter is for PFT 15 that only represents 20% of the PFTs at this site while
556 PFT 7 (boreal needleleaf evergreen forest) is the dominant PFT. This can be explained by the range of variation
557 that is assigned to f_{CA} of PFT 7 by Meredith et al. (2019), which is larger than the one of f_{CA} for PFT 15 (9000
558 against 3100).

559 Finally, a set of parameters related to photosynthesis, conductance, phenology, hydrology, and carbon uptake has
560 an impact on soil COS fluxes computed with both the empirical and the mechanistic models at the two sites. The
561 specific leaf area (SLA), maximum rate of Rubisco activity-limited carboxylation at 25°C ($V_{\text{cmax}25}$), residual
562 stomatal conductance (g_0) and minimum photosynthesis temperature (T_{min}) have an impact on soil COS fluxes
563 as they also indirectly affect soil moisture through their influence on transpiration and stomatal opening. The
564 second-order parameters related to soil hydrology (a , K_s , Z_{root} , θ_{WP} , θ_{FC} , θ_{R} , $\theta_{\text{Transp_max}}$) impact the soil
565 water availability, which affects soil respiration for the empirical model and soil COS diffusion and uptake in the
566 mechanistic model. For example, the parameter for root profile (Z_{root}) determines the density and depth of the
567 roots, and therefore how much water can be taken up by roots.

568 3.1.5 Soil COS flux optimization

569 Figure 6 presents soil COS fluxes before and after optimization of the model parameters to better fit the
570 observations at FI-HYY and US-HA. For the mechanistic model, the optimization at the two sites mainly changes
571 the mean value of soil COS fluxes, by reducing the net uptake at US-HA and increasing it at FI-HYY. Similar to
572 the mechanistic model optimization, the posterior soil COS uptake computed with the empirical model is enhanced
573 at FI-HYY and reduced at US-HA. However, at US-HA, the increase in soil COS uptake is only found between
574 April and October, while the winter soil COS fluxes are not impacted by the optimization. Using the optimized
575 parameterization improves the RMSD by 7% and 5% at US-HA and by 23% and 25% at FI-HYY for the
576 mechanistic and the empirical model, respectively. While it leads to similar posterior RMSD values between the
577 two models at US-HA, the optimization of the mechanistic model gives a lower RMSD than the empirical model
578 at FI-HYY, with $0.54 \text{ pmol m}^{-2} \text{ s}^{-1}$ against $0.95 \text{ pmol m}^{-2} \text{ s}^{-1}$.

579 At FI-HYY, the difference between prior and posterior soil COS fluxes from the empirical model seems to mainly
580 come from the change in soil_Q10 value (Appendix E, Figure E1). soil_Q10 value drops from 0.83 to 0.53, which
581 corresponds to a prior Q10 value of 2.29 versus a posterior value of 1.70, decreasing the heterotrophic respiration
582 response to soil temperature. Soil COS fluxes computed with the empirical model were found to be strongly
583 sensitive to soil_Q10 (Figure 5). The posterior value of this parameter has nearly attained the lower bound of its
584 variation range. Since the range of variation represents the realistic values this parameter can take, we need to be



585 careful about the fact that this parameter is trying to take values close to, or potentially beyond, these meaningful
586 values. Furthermore, the optimization deviates the Q10 value at FI-HYY from the ones calculated in the
587 observations over the measurement period (3.0 for soil chamber 1 and 2.5 for soil chamber 2). We could assume
588 that k_{soil} should be defined as temperature-dependent for linking soil COS flux to soil respiration (Berkelhammer
589 et al., 2014; Sun et al., 2018), instead of being considered as a constant. Thus, the optimization of the empirical
590 model could in fact be aliasing the error of k_{soil} onto soil_Q10 because of the impossibility to account for the
591 temperature-dependence of soil COS to CO₂ uptake ratio (Sun et al., 2018). At US-HA, the optimization also leads
592 to a decrease of soil_Q10 but to a lesser extent, the parameter remaining comfortably within its range of variation.
593 For the mechanistic model, the optimization reduces the enhancement factor value (f_{CA}) for PFT 10 at US-HA and
594 increases the value of the production parameter α for the dominant PFT (PFT 6). This enhances the reduction in
595 net soil COS uptake, which was slightly overestimated with the prior model parametrization. At FI-HYY, the
596 optimized parameters show higher values of f_{CA} and of α for PFT 15, and of both production parameters (α and
597 β) for the dominant PFT (PFT 7). This increase in both soil COS uptake and production after optimization could
598 correspond to an attempt to better simulate the larger range of variation found in the observations compared to the
599 modelled fluxes.

600 Finally, the optimization also affects hydrology-related parameters for both models. However, while it improves
601 the simulated water content compared to the observations for the mechanistic model at the two sites, it leads to a
602 degradation at FI-HYY for the empirical model (not shown). Since the empirical model is quite a simplistic model
603 with few parameters, it relies on parameters from different processes to help better fit the observations – sometimes
604 degrading the fit to the other processes. The mechanistic model is able to both improve the fit to the COS
605 observations and soil moisture values implying its parameterization is more consistent.

606 This optimization experiment has been promising, highlighting how observations can be used to improve the
607 models. However, since we only optimized over two sites due to the scarcity of soil COS flux observations, for
608 the global scale simulations in the rest of this study, we will rely on the default parameter values of each
609 parameterization.

610 3.2 Global scale COS fluxes

611 3.2.1 Soil COS fluxes

612 The spatial distribution of oxic soil COS fluxes shows a net soil COS uptake everywhere except in India, in the
613 Sahel region and some areas in the tropical zone, where net soil COS production is simulated (Figure 7a). The
614 strongest uptake rates are found in Western North and South America, and in China, with a mean maximum uptake
615 of $-4.4 \text{ pmol COS m}^{-2} \text{ s}^{-1}$ over 2010-2019. The difference in magnitude between the maximum uptake value and
616 the maximum of production can be noticed, with a net production reaching $67.2 \text{ pmol COS m}^{-2} \text{ s}^{-1}$ in the Sahel
617 region. India and the Sahel region, where oxic soil COS production is concentrated, are represented in ORCHIDEE
618 by a high fraction of C₃ and C₄ crops (Figure S3). In the mechanistic model, crops are associated with the lowest
619 f_{CA} value due to overall lower fungal diversity and abundance in agricultural fields (Meredith et al., 2019), and the
620 strongest response of oxic soil COS production to temperature as observed by Whelan et al. (2016). Thus, these
621 PFT-specific parameters combined with high temperature in the tropical region can explain the net oxic soil COS
622 production found in these regions. C₃ crops are also dominant in China near the Yellow Sea (Figure S3). However,
623 the mean soil temperature in this region is about 15°C lower than the mean soil temperature in India, leading to a



624 lower enhancement of soil COS production. The highest atmospheric COS concentration is also found in this
625 region with about 800 ppt (Figure S2). Indeed, recent inventories have shown that China was related to strong
626 anthropogenic COS emissions due to the industry, biomass burning, coal combustion, agriculture, or vehicle
627 exhaust (Yan et al., 2019; Zumkehr et al., 2018). High atmospheric COS concentrations increase soil COS
628 diffusion and uptake that can compensate part of soil COS production. The highest values of soil COS fluxes for
629 anoxic soils are located in northern India, with a mean maximum value reaching $36.8 \text{ pmol COS m}^{-2} \text{ s}^{-1}$ (Figure
630 7b). This region is characterized by rice paddies, which were also associated with strong COS production in
631 previous studies (Zhang et al., 2004).

632 The total soil COS fluxes (oxic and anoxic) computed with the mechanistic model (Figure 7c) show a very different
633 spatial distribution than the one obtained with the empirical model (Figure 7d). Soil COS fluxes from the empirical
634 model are on the same order of magnitude for net COS uptake than the mechanistic model, with a mean maximum
635 uptake of $-6.41 \text{ pmol COS m}^{-2} \text{ s}^{-1}$. However, most soil COS uptakes simulated by the empirical model is located
636 in the tropical region, where soil respiration is strong due to high temperature.

637 The difference of soil COS fluxes between the mechanistic model and the empirical model ranges from -4.1 pmol
638 $\text{COS m}^{-2} \text{ s}^{-1}$ to $+68.0 \text{ pmol COS m}^{-2} \text{ s}^{-1}$ (Appendix D, Figure D1). Over western North and South America, northern
639 and southern Africa, western Asia, and eastern, northern and Central Asia, the net COS uptake from the
640 mechanistic model exceeds the uptake from the empirical model. On the contrary, soil COS uptake from the
641 empirical approach is higher than the net COS uptake simulated with the mechanistic model over Eastern North
642 and South America, Western, Central and Eastern Africa, and Indonesia. The absence of soil COS production
643 representation in the empirical approach leads to the strongest differences in India and in the Sahel region, reaching
644 $+68.0 \text{ pmol COS m}^{-2} \text{ s}^{-1}$.

645 3.2.2 Temporal evolution of the soil COS budget

646 We computed the mean annual soil COS budget over the period 2010-2019 using the monthly variable atmospheric
647 COS concentration and we compared its evolution to the variations of the mean annual atmospheric COS
648 concentration.

649

650 The evolution of the mean annual soil COS budget (Figure 8) shows small variations in the budget for oxic soils
651 computed with the mechanistic model between 2010 and 2015, with a net sink ranging from -133 GgS y^{-1} to -124
652 GgS y^{-1} . Then, from 2016 we see a sharp decrease in this budget, which reaches -98 GgS y^{-1} in 2019. This decrease
653 also corresponds to the decrease in atmospheric COS concentration observed between 2016 and 2019 with a loss
654 of 25 ppt in 3 years. It is worth noting that other monitoring stations recorded a drop in atmospheric COS
655 concentration over Europe, as for the GIF station with -42 ppt between 2015 and 2021 (updated after Belviso et
656 al., 2020). On the contrary, the soil COS net uptake computed with the empirical model slightly increases
657 from -212 GgS y^{-1} in 2010 to -219 GgS y^{-1} in 2019. As the empirical model defines soils COS flux as proportional
658 to the total soil respiration independently of atmospheric COS concentration, the budget obtained with this model
659 is not impacted by the variations observed in atmospheric COS concentration. The anoxic soil COS budget follows
660 soil temperature variations (not shown), with an increasing trend of about 0.17 GgS yr^{-1} over the studied period.



661 **3.3 Transport and site-scale concentrations**

662 **Interhemispheric gradient**

663 We transported total COS fluxes for the different configurations (i.e. including the soil fluxes but also other
664 components of the COS atmospheric budget, listed in Table 2) with the LMDZ6 atmospheric transport model as
665 described in Sect. 2.1.3. We analyzed COS concentrations derived from simulated COS fluxes obtained with the
666 mechanistic and two empirical approaches with regards to the COS concentrations observed at 14 NOAA sites
667 depicted in Appendix B, Fig. B1. Note that atmospheric mixing ratios of COS result from the transport of all COS
668 sources and sinks and that, due to other sources of errors (transport and errors in the other COS fluxes), the
669 comparison presented in the following should be taken as a sensitivity study of COS seasonal cycle and inter-
670 hemispheric gradient to the soil exchange fluxes rather than a complete validation of one approach or the other.
671 Figure 9: shows the COS atmospheric concentrations at NOAA sites as a function of latitude for each simulated
672 soil flux and for the observations. Here as we want to focus on the latitudinal variations of atmospheric COS
673 mixing ratios, the atmospheric COS concentrations have been vertically shifted to have the same mean as the
674 observations. This means that the concentrations values cannot be compared at each site, we can only compare the
675 interhemispheric gradients of simulated and observed concentrations. The RMSD for the mechanistic model with
676 oxic soils only, the mechanistic model with oxic and anoxic soils, the empirical Berry model (with oxic soils only),
677 and the empirical Launois model (with oxic and anoxic soils) are 36.5, 39.4, 43.0, 51.0 ppt, respectively. While
678 the different approaches show similar gradient patterns in the southern latitudes, they lead to strong differences in
679 the simulated concentrations in the northern hemisphere. Compared to empirical approaches, the mechanistic
680 approach marginally improves the latitudinal distribution of the atmospheric mixing ratios by decreasing the
681 concentrations in the high latitudes. The lower atmospheric mixing ratios above 60 °N reflect the stronger soil
682 absorption in the mechanistic model (see Figure 9), where soil COS uptake is dominant and the compensation by
683 COS production is small (Appendix D, Figure D2). Despite this slight improvement, there are persistent biases as
684 overestimated concentrations at the high latitude sites ALT, BRW, SUM, and underestimated concentrations at
685 most tropical sites: WIS, MLO and SMO. These model-observation mismatches have led top-down studies to
686 identify the missing source as being the tropical oceanic emissions (Berry et al., 2013; Launois et al., 2015;
687 Remaud et al., 2021; Davidson et al., 2021). The present anoxic soil fluxes have little impact on the surface
688 latitudinal distributions and therefore are unlikely to shed new light on the tropical missing source. An explanation
689 for the small impact is that they are located outside areas experiencing deep convection events (e.g. the Indian
690 monsoon domain) and thus the surface concentrations are less sensitive to these fluxes.

691 **Seasonal cycle at NOAA sites**

692 Figure 10 shows the detrended temporal evolution of COS concentrations for the mechanistic and empirical
693 approaches at Alert (ALT, Canada) and Harvard Forest (HFM, USA). Because of the mean westerly flow, the
694 HFM site is influenced by continental regions to the west (Sweeney et al., 2015), and is more sensitive to the soil
695 fluxes than other mid-latitude sites located to the west of the ocean (MHD, THD), see Fig. 1 in Remaud et al.
696 (2021). The ALT site samples air masses coming from high-latitude ecosystems (Peylin et al., 1999), but also from
697 regions further south due to atmospheric transport (Parazoo et al., 2011). The reader is referred to Appendix B,
698 Table B2 for the other sites. At both sites, the mechanistic approach tends to weaken the total seasonal amplitude
699 and increase the model-data mismatch. At ALT, the seasonal amplitude is marginally decreased, while at HFM it



700 is divided by two. At ALT, BRW and SUM, the too high atmospheric concentrations and the too weak seasonal
701 amplitude given by the mechanistic approach are consistent with an underestimated soil absorption at sites ET-JA
702 (Estonia) and FI-HYY (Finland) (see Figure 2). As for Harvard Forest, since the mechanistic soil model shows
703 overall good agreement with the observed soil fluxes (e.g. Figure 2), the model-observation mismatch likely arises
704 from errors in other components of the COS budget (in particular oceanic and vegetation fluxes). Therefore,
705 empirical approaches give a more realistic seasonality of atmospheric concentrations for the wrong reasons, which
706 likely hides an underestimated vegetation uptake. Indeed, as Maignan et al. (2021) showed that the vegetation
707 uptake magnitude in ORCHIDEE was consistent with measurements, the introduction of variable atmospheric
708 COS concentrations decreased the vegetation uptake, which as a result, is very likely underestimated now.
709 Moreover, the comparison between simulated and observed concentrations show a degradation of the simulated
710 concentrations in this study compared to Maignan et al. (2021). It is to be noted that in addition to using a variable
711 atmospheric COS concentration in this study, the transported ocean COS fluxes from Masotti et al. (2016) and
712 Lennartz et al. (2017, 2021) differ from the ones used in Maignan et al. (2021), from Kettle et al. (2002) and
713 Launois et al. (2015). These results illustrate the necessity of well constraining both the soil and vegetation fluxes
714 in order to optimize the GPP with the help of atmospheric inverse modelling.

715 **4 Discussion**

716 **4.1 Soil budget**

717 According to the mechanistic approach of this study, the COS budget for oxic soil is a net sink of -126 GgS yr^{-1}
718 over 2009-2016, which is close to the value of -130 GgS yr^{-1} found by Kettle et al. (2002) (Table 5). The
719 mechanistic model gives the lowest oxic soil COS net uptake compared to all previous studies using empirical
720 approaches. This budget is also 41% lower than the one found with the Berry empirical approach in this study,
721 with an uptake of -214 GgS yr^{-1} . The anoxic soil COS budget computed with the mechanistic approach is $+96 \text{ GgS}$
722 yr^{-1} , which is close to the budget found by Launois et al. (2015) of $+101 \text{ GgS yr}^{-1}$ based on methane emissions.
723 However, while COS emissions from anoxic soils were only located in the northern latitudes in Launois et al.
724 (2015), the COS production in this study is also distributed in the tropical region. Thus, we can expect that despite
725 similar budget values for anoxic soils, the difference in flux distribution will impact the latitudinal gradient of COS
726 fluxes. Finally, adding anoxic soil COS budget to oxic soil COS budget results in a total soil COS budget of only
727 -30 GgS yr^{-1} for the mechanistic approach.

728 When computing the net total COS budget considering all sources and sinks of COS, the net total from the
729 empirical approach is closer to zero (-35 GgS yr^{-1}) than the net total from the mechanistic model ($+149 \text{ GgS yr}^{-1}$).

730 In the empirical approach, neglecting the potential COS production of oxic soils and COS emissions from anoxic
731 soils leads to a small overestimation of COS sink or underestimation of COS source to close the budget. On the
732 contrary, the mechanistic approach leads to an overestimation of COS source or an underestimation of COS sink
733 components. This positive net global budget could be due to an underestimation of vegetation COS uptake in the
734 northern hemisphere, participating in the underestimation of the COS concentration drawdown (Figure 9), but the
735 absence of anthropogenic emission seasonality could also play a role. The two net totals obtained in this study are
736 closer to closing the COS budget than the previous approach from Launois et al. (2015).

737 Despite a net COS budget closer to zero with the empirical model, it is to be noted that the mechanistic model
738 better simulates the lack of seasonality at US-HA compared to the empirical model (Figure 2). US-HA is



739 represented by 80% of PFT6 (temperate broadleaved summergreen forest) and the absence of seasonality by this
740 PFT has also been reported at a mid-latitude site at Gif-sur-Yvette (Belviso et al., 2020). This PFT is largely found
741 in the temperate region such as in Europe and in the southern United-States. Moreover, NWR, HFM and LEF
742 stations are mainly influenced by COS exchanges from the PFT6. Therefore, the use of the mechanistic model
743 would be recommended to carry out new comparisons at these mid-latitude sites.

744 4.2 Variable atmospheric COS concentration versus constant atmospheric COS concentration

745 We studied the impacts of using a constant versus a variable atmospheric COS concentration on soil COS fluxes.
746 At the site-scale we found a distinction between the sites where soil COS production is strong (IT-CRO and ES-
747 LMA) and the sites mainly showing a net soil COS uptake. The impact of using a constant atmospheric COS
748 concentration is lower at IT-CRO and ES-LMA because the atmospheric COS concentration does not directly
749 impact the soil COS production term but participates in the net soil COS flux. Our study shows that at the sites
750 where a net soil COS uptake is dominant, using a constant atmospheric COS concentration leads to an
751 underestimation of soil COS flux in winter and an overestimation of soil COS flux from spring to autumn (not
752 shown). Indeed, during the growing season, plant uptake decreases atmospheric COS concentration (Figure S1),
753 which reduces COS availability for soil COS diffusion, whereas during winter, a higher atmospheric COS
754 concentration enhances COS diffusion into the soil.

755 At the global scale, as the variable atmospheric COS concentration used in this study shows a decrease of about
756 25 ppt in the recent years (Figure 8), considering a constant atmospheric COS concentration would not enable to
757 represent the impact of this strong variation on soil COS fluxes. When computing the soil COS budget over 2016
758 to 2019, we found a net uptake of -126 GgS yr^{-1} with the mechanistic model using a constant atmospheric COS
759 concentration, against the -110 GgS yr^{-1} computed with a monthly spatially variable concentration. Using a
760 constant atmospheric COS concentration would then lead to an overestimation of about 13% of the net soil COS
761 uptake over the past 4 years.

762 We also studied the impact of considering a constant versus a variable atmospheric COS concentration on the
763 seasonal variations of mean monthly soil COS fluxes over 2010-2019, simulated with the mechanistic model (not
764 shown). We found that using a constant atmospheric COS concentration leads to an overestimation of net soil COS
765 uptake over the whole year in the southern latitudes and from June to February in the northern latitudes (reaching
766 $1.62 \text{ pmol m}^{-2} \text{ s}^{-1}$). This overestimation increases over the regions with the lowest atmospheric COS concentrations,
767 which limits COS diffusion through the soil matrix. On the contrary when atmospheric COS concentration is high
768 in the northern latitudes between April and May, considering a constant atmospheric COS concentration leads to
769 an underestimation of net soil COS uptake. We notice that this underestimation with a constant atmospheric COS
770 concentration can be found as early as March over Europe, where atmospheric COS concentration is higher in this
771 region. In eastern Asia, where atmospheric COS concentration is higher than 800 ppt, the underestimation of the
772 net soil COS uptake can reach $-2.34 \text{ pmol m}^{-2} \text{ s}^{-1}$ when considering a constant atmospheric COS concentration.

773 It is to be noted that the modelled COS concentrations we used have their own uncertainty, which is however
774 smaller than their difference with the fixed value (Remaud et al., 2021).



775 4.3 Foreseen improvements

776 The mechanistic representation of soil COS fluxes was found to be in better agreement with the observations at
777 field sites. However, there can be strong differences between the simulated fluxes and the observations at some
778 sites, especially at AT-NEU and ES-LMA. In the mechanistic approach, the influence of light on soil COS fluxes
779 is not considered. Several field studies have reported light-induced emissions in oxic soils (Kitz et al., 2017;
780 Meredith et al., 2018; Spielmann et al., 2019; Whelan and Rhew, 2015), assumed to be related to the effect of light
781 on soil organic matter. Spielmann et al. (2019) related strong soil COS emissions during daytime to light at the
782 sites where direct solar radiations reached the surface, such as ES-LMA and AT-NEU. At these sites, the
783 mechanistic model was unable to represent the soil COS emission peak during daytime. The optimization we
784 performed showed that, as expected, adjusting the parameters to site observations improves the fit between the
785 simulated and observed fluxes. However, it is necessary to represent all important processes in the mechanistic
786 approach before calibrating the parameters. Thus, a next step in our modelling approach could be to include the
787 light influence on soil COS fluxes, which can be of major importance for the sites where radiations strongly affect
788 soil COS fluxes. Mellillo and Steudler (1989) also found that soil COS production could be related to nitrogen
789 content, which increases with nitrogen fertilizer application. Then crop management practices might also need to
790 be included when representing the dynamics of soil COS fluxes.

791 Moreover, one difficulty with the study of soil COS fluxes arises from the scarcity of field measurements that
792 could be used for data assimilation. Therefore, more field measurements would help to build a larger field
793 observation database for model validation and calibration. In particular, the characterization of the soil microbial
794 community should also be addressed to improve the scaling of CA content and activity, represented by the f_{CA}
795 parameter (Meredith et al., 2019).

796 The mechanistic model from Ogée et al. (2016) has also recently been implemented in the LSM SiB4 (Kooijmans
797 et al., 2021). In SiB4, the simulated soil COS fluxes with the mechanistic model show a seasonal cycle with a
798 maximum net soil COS uptake in summer for the sites without crops, while the fluxes computed in ORCHIDEE
799 show almost no seasonality. The expression of the production term P differs between the two models, which is
800 based on Meredith et al. (2018) in SiB4 and on Whelan et al. (2016) in ORCHIDEE. The observation sites that are
801 common to the two studies (FI-HYY, US-HA, AT-NEU and DK-SOR) are also represented by different fractions
802 of biomes between SiB4 and ORCHIDEE, which changes the parameterization to compute soil COS fluxes.
803 Finally, the parameter values for the enhancement factor f_{CA} for grass differ as the value for tropical grass is also
804 assigned to C_3 and C_4 grass in SiB4. Soil COS flux field data are mainly available in summer, therefore having
805 field measurements over a whole year could better inform the seasonality of observed soil COS fluxes to compare
806 to the simulations.

807 The optimization does not modify the respective seasonality of both soil COS models, with a seasonal cycle that
808 agrees with the one of soil respiration for the empirical model and a lack of seasonality for the mechanistic model.

809 The lack of observations in winter does not enable to constrain soil COS fluxes in winter. Therefore, having field
810 observations over a whole year could help to determine if both models could be calibrated with a constrain over
811 the whole year instead of only during summer and autumn. Moreover, the optimized set of parameters for the
812 empirical models leads to a degradation of the simulated soil water content compared to the observations at FI-
813 HYY, while the optimized parameters of the mechanistic model improve the representation of soil water content



814 at US-HA and FI-HYY. Thus, the mechanistic approach is to be preferred over the empirical model and should be
815 selected for future COS studies in ORCHIDEE.

816 The sensitivity analyses showed the importance of the hydrology-related parameters in the computation of soil
817 COS fluxes with the mechanistic model. Thus, assuming an accurate representation of soil COS fluxes, soil COS
818 fluxes could have the potential to add a new constraint on hydrology-related parameters.

819 In this work, soil COS fluxes are computed in the top 9 cm, which assumes that soil COS uptake and production
820 depend on the conditions in the first soil layers. Indeed, soil COS uptake depends on diffusive supply of COS from
821 the atmosphere. However, since soil COS production does not depend on COS supply, deeper soil layers could
822 also contribute to soil COS production. A study by Yang et al. (2019) presents COS profile measurements in an
823 orchard, which shows a non-zero COS concentration in deeper soil layers, but no direct evidence for attributing it
824 to soil COS production. Thus, we could consider deeper soil layers in the future to study the impact on soil COS
825 fluxes compared to considering only the top soil layers.

826 The anoxic soil map of regularly flooded wetlands from Tootchi et al. (2019) enables to approximate the spatial
827 distribution of anoxic soil. However, in our approach, seasonality is only represented through soil temperature
828 seasonality. Anoxic soil temporal dynamic was initially included in the model described by Ogée et al. (2016) with
829 the soil redox potential but is not implemented in land surface models such as ORCHIDEE yet. We could also
830 refine our approach by distinguishing between the different types of wetlands and define a P_{ref} value for each
831 wetland type instead of a global value of $10 \text{ pmol COS m}^{-2} \text{ s}^{-1}$. Moreover, indirect COS emissions from DMS
832 oxidation in anoxic soils have been reported (Kettle et al., 2002; Watts, 2000) but are not represented in this study.
833 Finally, the anoxic map used here represents 9.7% of the global land area, but the distribution of anoxic soils can
834 greatly vary depending on the study (between 3% and 21%, Tootchi et al., 2019). Therefore, it would also be
835 interesting to investigate the impact of anoxic soil coverage on soil COS flux uncertainty.

836 5 Conclusions and Outlooks

837 We have implemented in the ORCHIDEE LSM a mechanistic and an empirical model for simulating soil COS
838 fluxes. The mechanistic model, that performs a spatialization of the Ogée et al. (2016) model, enables us to
839 consider that oxic soils can be net COS producers, as illustrated at some of the observation sites. The inter-
840 hemispheric gradient of COS surface atmospheric mixing ratio is marginally improved when all known COS
841 sources and sinks are transported with the LMDZ model. This study also highlights the sensitivity of simulated
842 atmospheric COS concentrations to soil COS flux representation in the northern latitudes. Thus, the uncertainty in
843 soil COS fluxes could complicate GPP estimation using COS in the northern hemisphere.

844 The soil COS budget at global scale over the 2009-2016 period is -30 GgS yr^{-1} , resulting from the contribution of
845 oxic soils that represent a net sink of -126 GgS yr^{-1} , and of anoxic soils that represent a source of $+96 \text{ GgS yr}^{-1}$. It
846 is to be noted that the contribution from anoxic soils, while leading to a similar global budget to Launois et al.
847 (2015), has a different spatial distribution based on the repartition of regularly flooded wetlands from Tootchi et al.
848 (2019). This repartition seems more accurate as it also includes anoxic soil COS flux in the tropical region and
849 considers a larger variety of anoxic soils, such as salt marshes and rice paddies.

850 During this work, we have also shown the importance of considering spatially and temporally variable atmospheric
851 COS concentrations on soil COS fluxes, with an especially large impact at global scale. This result evidences the
852 impact of the recently decreasing atmospheric COS concentrations on the estimated soil COS fluxes.



853 Regarding the ORCHIDEE model, we performed a sensitivity study highlighting the key parameters to optimize
854 for the soil models. The impact of soil model parameter optimization was studied at two sites. This study exhibited
855 strong arguments in favour of the mechanistic model as performing an optimization of the empirical model
856 parameters can lead to aliasing errors and a degradation of the simulated soil water content. A larger database of
857 COS flux measurements at the site scale and especially full year time series would greatly help for the next step,
858 which would be to optimize the parameters of ecosystem COS fluxes.



859 **Appendix A: Parameters, variables, and constants for soil COS models**

860

861 **Table A1: Carbonic anhydrase enhancement factor adapted to ORCHIDEE biomes.**

ORCHIDEE biomes	Biomes from Meredith et al. (2019)	f_{CA} value from Meredith et al. (2019) (unitless)
1 - Bare soil	Desert	13000 ± 5400
2 - Tropical broad-leaved evergreen	Temperate broadleaf forest	32000 ± 1800
3 - Tropical broad-leaved raingreen	Temperate broadleaf forest	32000 ± 1800
4 - Temperate needleleaf evergreen	Temperate coniferous forest	32000 ± 3100
5 - Temperate broad-leaved evergreen	Temperate broadleaf forest	32000 ± 1800
6 - Temperate broad-leaved summergreen	Temperate broadleaf forest	32000 ± 1800
7 - Boreal needleleaf evergreen	Temperate coniferous forest	32000 ± 3100
8 - Boreal broad-leaved summergreen	Temperate broadleaf forest	32000 ± 1800
9 - Boreal needleleaf summergreen	Temperate coniferous forest	32000 ± 3100
10 - C ₃ grass	Mediterranean grassland	17000 ± 9000
11 - C ₄ grass	Mediterranean grassland	17000 ± 9000
12 - C ₃ agriculture	Agricultural	6500 ± 6900
13 - C ₄ agriculture	Agricultural	6500 ± 6900
14 - Tropical C ₃ grass	Tropical grassland	45000
15 - Boreal C ₃ grass	Mediterranean grassland	17000 ± 9000

862

863



864 **Table A2: α and β parameters for COS production term adapted to ORCHIDEE biomes.**

ORCHIDEE biomes	Biomes from Whelan et al. (2016)	α parameter from Whelan et al. (2016) (unitless)	β parameter from Whelan et al. (2016) ($^{\circ}\text{C}^{-1}$)
1 - Bare soil	Desert	N/A	N/A
2 - Tropical broad-leaved evergreen	Rainforest	-8.2	0.101
3 - Tropical broad-leaved raingreen	Rainforest	-8.2	0.101
4 - Temperate needleleaf evergreen	Temperate forest	-7.77	0.119
5 - Temperate broad-leaved evergreen	Temperate forest	-7.77	0.119
6 - Temperate broad-leaved summergreen	Temperate forest	-7.77	0.119
7 - Boreal needleleaf evergreen	Temperate forest	-7.77	0.119
8 - Boreal broad-leaved summergreen	Temperate forest	-7.77	0.119
9 - Boreal needleleaf summergreen	Temperate forest	-7.77	0.119
10 - C ₃ grass	Savannah	-9.54	0.108
11 - C ₄ grass	Savannah	-9.54	0.108
12 - C ₃ agriculture	Soy field	-6.12	0.096
13 - C ₄ agriculture	Soy field	-6.12	0.096
14 - Tropical C ₃ grass	Savannah	-9.54	0.108
15 - Boreal C ₃ grass	Savannah	-9.54	0.108

865
 866
 867
 868



869 **Table A3: Variables for the empirical and mechanistic COS soil models.**

Variable name	Description	Unit	Reference
Empirical COS soil model			
$F_{soil,empirical}$	Empirical model soil COS flux	pmol COS m ⁻² s ⁻¹	(Berry et al., 2013) (Yi et al., 2007b)
$Resp_{tot}$	Total (heterotrophic and autotrophic) soil respiration	μmol CO ₂ m ⁻² s ⁻¹	(Yi et al., 2007b)
Mechanistic COS soil model			
ϵ_{tot}	Total soil COS porosity	m ³ air m ⁻³ soil	(Ogée et al., 2016)
C	Soil COS concentration	mol m ⁻³	(Ogée et al., 2016)
F_{diff}	Soil COS diffusional flux	mol m ⁻² s ⁻¹	(Ogée et al., 2016)
S	Soil COS consumption rate	mol m ⁻³ s ⁻¹	(Ogée et al., 2016)
P	Soil COS production rate	mol m ⁻³ s ⁻¹	(Whelan et al., 2016)
$F_{soil,mechanistic}$	Mechanistic model soil COS flux	mol m ⁻² s ⁻¹	(Ogée et al., 2016)
k	Total COS consumption rate by soil	s ⁻¹	(Ogée et al., 2016)
B	Solubility of COS in soil water	m ³ water m ⁻³ air	(Ogée et al., 2016)
θ	Soil volumetric water content	m ³ water m ⁻³ soil	(Ogée et al., 2016)
D	Total effective COS diffusivity in soil	m ² s ⁻¹	(Ogée et al., 2016)
z_1	Characteristic deep for soil COS flux	m	(Ogée et al., 2016)
k_{uncat}	Uncatalysed rate of COS hydrolysis in the soil water	s ⁻¹	(Elliott et al., 1989)
k_{cat}	Turnover rate of COS enzymatic reaction catalyzed by CA	s ⁻¹	(Ogée et al., 2016)
K_m	Michaelis-Menten constant of CA catalysis	mol m ⁻³	(Ogée et al., 2016)
x_{CA}	Temperature dependence of the ratio k_{cat}/K_m	1	(Ogée et al., 2016)



k	Soil total COS consumption rate	s^{-1}	(Ogée et al., 2016)
f_{CA}	CA enhancement factor	1	(Meredith et al., 2019)
$D_{eff,a}$	Effective diffusivity of gaseous COS in soil	$m^3 \text{ air } m^{-1} \text{ soil } s^{-1}$	(Ogée et al., 2016)
$D_{eff,l}$	Effective diffusivity of dissolved COS in soil	$m^3 \text{ water } m^{-1} \text{ soil } s^{-1}$	(Ogée et al., 2016)
K_H	Henry's law constant	$mol \text{ m}^{-3} \text{ Pa}^{-1}$	(Bird et al., 2002)
$D_{0,a}$	Binary diffusivity of COS in the free air	$m^2 \text{ air } s^{-1}$	(Bird et al., 2002)
τ_a	Tortuosity factor for gaseous diffusion	1	(Ogée et al., 2016)
$\tau_{a,r}$	Tortuosity factor for gaseous diffusion in repacked soils	1	(Moldrup et al., 2003)
$\tau_{a,u}$	Tortuosity factor for gaseous diffusion in undisturbed soils	1	(Deepagoda et al., 2011)
$D_{0,l}$	Binary diffusivity of COS in the free water	$m^2 \text{ water } s^{-1}$	(Zeebe, 2011)
τ_l	Tortuosity factor for solute diffusion	1	(Millington and Quirk, 1961)
α	COS production parameter	1	(Whelan et al., 2016)
β	COS production parameter	1	(Whelan et al., 2016)
ORCHIDEE LSM			
p	Pressure		ORCHIDEE LSM
ε_a	Air-filled porosity	$m^3 \text{ air } m^{-3} \text{ soil}$	ORCHIDEE LSM
φ	Total soil porosity (air-filled and water-filled pores)	$m^3 \text{ m}^{-3}$	ORCHIDEE LSM
T	Mean soil temperature	K	ORCHIDEE LSM



t	time	s	ORCHIDEE LSM
---	------	---	--------------

z	depth	m	ORCHIDEE LSM
---	-------	---	--------------

870

871



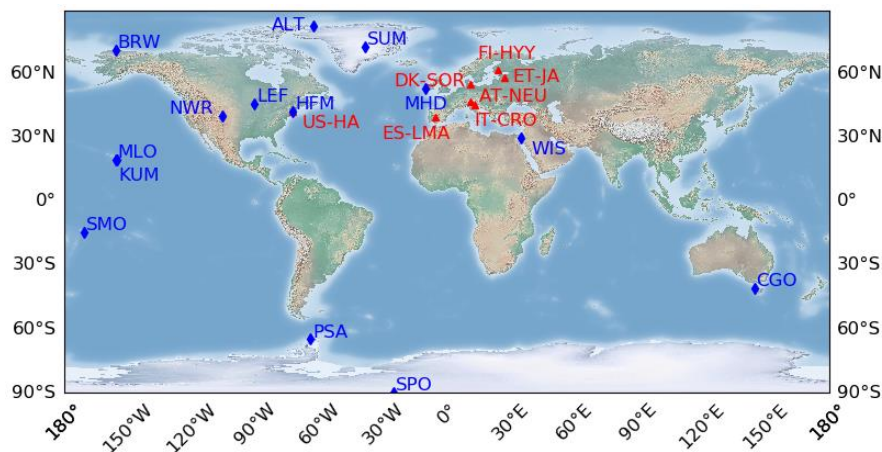
872 **Table A4: Constants for the empirical and mechanistic COS soil models.**

Constant name	Description	Value	Unit	Reference
Empirical COS soil model				
k_{soil}	Constant to converts CO ₂ production from respiration to a COS uptake	1.2	pmol COS/μmol CO ₂	(Yi et al., 2007)
Mechanistic COS soil model				
C_a	Ambient air COS concentration when chosen constant (500 ppt)	2.0437×10^{-8}	mol m ⁻³	
z_{max}	Maximum soil depth	0.09	m	ORCHIDEE LSM
pK_w	Dissociation constant of water	14	1	
ΔH_a	Thermodynamic parameter	40	kJ mol ⁻¹	(Ogée et al., 2016)
ΔH_d	Thermodynamic parameter	200	kJ mol ⁻¹	(Ogée et al., 2016)
ΔS_d	Thermodynamic parameter	660	J mol ⁻¹ K ⁻¹	(Ogée et al., 2016)
R	Ideal gas constant	8.314	J mol ⁻¹ K ⁻¹	
$D_{0,a}(25^\circ C, 1 atm)$	Binary diffusivity of COS in the free air at 25°C and 1 atm	1.27×10^{-5}	m ² s ⁻¹	(Massman, 1998)
$D_{0,l}(25^\circ C)$	Binary diffusivity of COS in the free water at 25°C	1.94×10^{-9}	m ² s ⁻¹	(Ulshöfer et al., 1996)
Q_{10}	Multiplicative factor of the production rate for a 10 °C temperature rise	2.7	1	(Meredith et al., 2018)
P_{ref}	Reference production term	10	pmol m ² s ⁻¹	



874 **Appendix B: Locations and descriptions of the observation sites**

875



876

877 **Figure B1: Locations of the observation sites for soil COS flux measurements (red) and atmospheric concentration**
 878 **measurements (blue).**

879

880 **Table B1: List of air sampling sites selected for evaluation of COS concentrations.**

Site	Short name	Coordinates	Elevation (m above sea level)	Comments
South Pole, Antarctica, United States	SPO	90.0°S, 24.8°E	2810	
Palmer Station, Antarctica, United States	PSA	64.77°S, 64.05°W	10.0	
Cape Grim, Australia	CGO	40.68°S, 144.69°E	164	inlet is 70 m aboveground
Tutuila, American Samoa	SMO	14.25°S, 170.56°W	77	
Mauna Loa, United States	MLO	19.54°N, 155.58°W	3397	
Cape Kumukahi, United States	KUM	19.74°N, 155.01°W	3	
Weizmann Institute of Science at the Arava Institute, Ketura, Israel	WIS	29.96°N, 35.06°E	151	
Niwot Ridge, United States	NWR	40.04°N, 105.54°W	3475	
Harvard Forest, United States	HFM	42.54°N, 72.17°W	340	inlet is 29 m aboveground
Wisconsin, United States	LEF	45.95°N, 90.28°W	868	inlet is 396 m aboveground on a tall tower



Mace Head, Ireland	MHD	53.33°N, 9.9°W	18	
Barrow, United States	BRW	71.32°N, 155.61°W	8	
Summit, Greenland	SUM	72.6°N, 38.42°W	3200	
Alert, Canada	ALT	82.45°N, 62.51°W	195	

881

882

883 **Table B2: Normalized standard deviations (NSDs) of the simulated concentrations by the observed concentrations.**
 884 **Within brackets are the Pearson correlation coefficients (r) between simulated and observed COS concentrations for**
 885 **the mechanistic and empirical approaches, calculated between 2011 and 2015 at selected NOAA stations. For each**
 886 **station, NSD and r closest to one are in bold and farthest ones are in italic. The time-series have been detrended**
 887 **beforehand and filtered to remove the synoptic variability (see Sect. 2.3.3).**

	SMO	KUM	MLO	NWR	LEF	HFM	MHD	SUM	BRW	ALT
Mechanistic	1.1	0.7	0.9	<i>0.4</i>	<i>0.2</i>	<i>0.3</i>	<i>1.5</i>	<i>0.4</i>	1.1	<i>0.8</i>
(Oxic)	(0.8)	(0.7)	(0.8)	<i>(0.4)</i>	<i>(0.7)</i>	(0.8)	(0.2)	(0.2)	<i>(0.1)</i>	<i>(0.1)</i>
Empirical	1.0	0.8	1.2	0.8	0.5	0.6	1.5	0.5	<i>1.3</i>	0.9
(Oxic)	(0.7)	(0.9)	(0.9)	(0.4)	(0.9)	(0.9)	(0.4)	(0.6)	(0.3)	(0.4)
Mechanistic	<i>1.2</i>	<i>0.6</i>	0.9	0.5	<i>0.2</i>	<i>0.3</i>	1.0	<i>0.4</i>	<i>1.3</i>	<i>0.8</i>
(Oxic+Anoxic)	(0.7)	<i>(0.6)</i>	<i>(0.7)</i>	(0.1)	<i>(0.2)</i>	<i>(0.5)</i>	<i>(0.1)</i>	<i>(0.0)</i>	<i>(0.1)</i>	<i>(0.1)</i>
Launois	1.1	1.0	<i>1.4</i>	1.4	0.9	0.8	1.6	0.6	1.2	0.9
(Oxic+Anoxic)	<i>(0.6)</i>	(0.9)	(0.9)	(0.7)	(0.9)	(0.9)	(0.4)	(0.7)	(0.4)	(0.4)

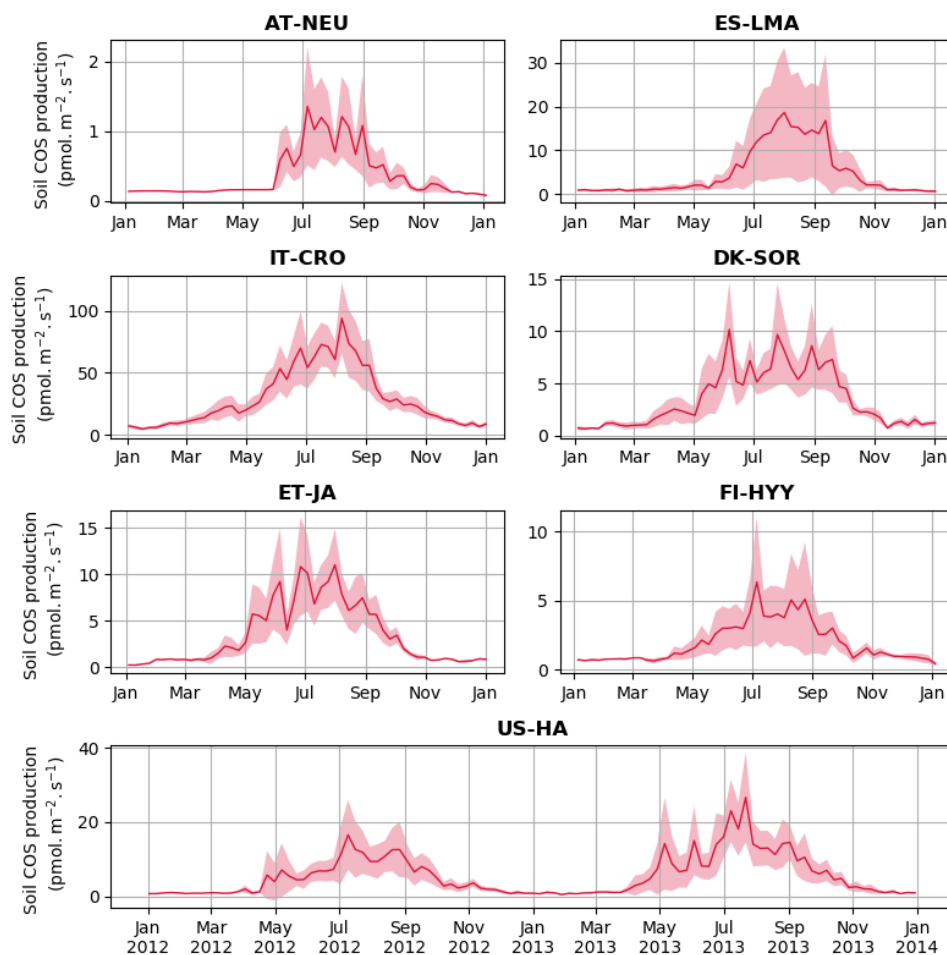
888

889



890 **Appendix C: Soil COS production term for the mechanistic model**

891



892

893 **Figure C1: Seasonal cycles of soil COS production with weekly average production at AT-NEU, ES-LMA, IT-CRO,**
894 **DK-SOR, ET-JA, FI-HYY, US-HA. The shaded areas above and below the modelled curve represent the standard-**
895 **deviation over a week. Soil COS production was computed with a variable atmospheric COS concentration.**

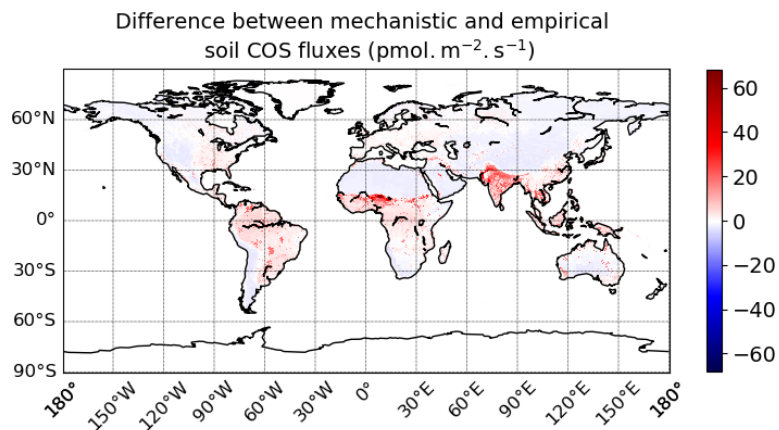
896

897



898 **Appendix D: Global scale soil COS fluxes**

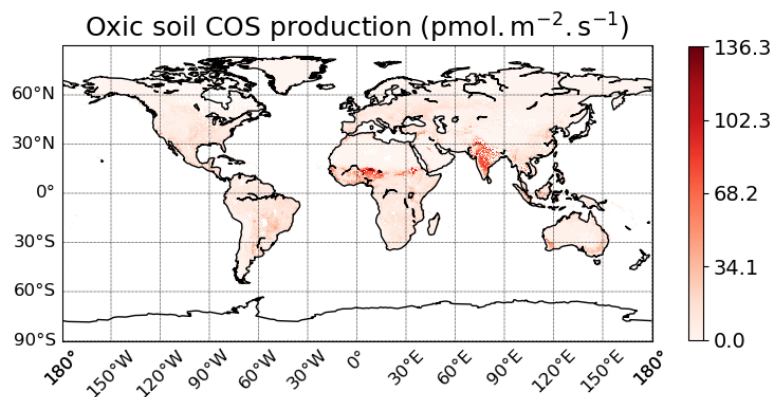
899



900

901 **Figure D1: Mean difference between soil COS fluxes computed with the mechanistic and the empirical model over 2010-**
902 **2019. The map resolution is 0.5°x0.5°.**

903



904

905 **Figure D2: Mean spatial distribution of oxic soil COS production term over 2010-2019. The map resolution is 0.5°x0.5°.**

906

907

908

909

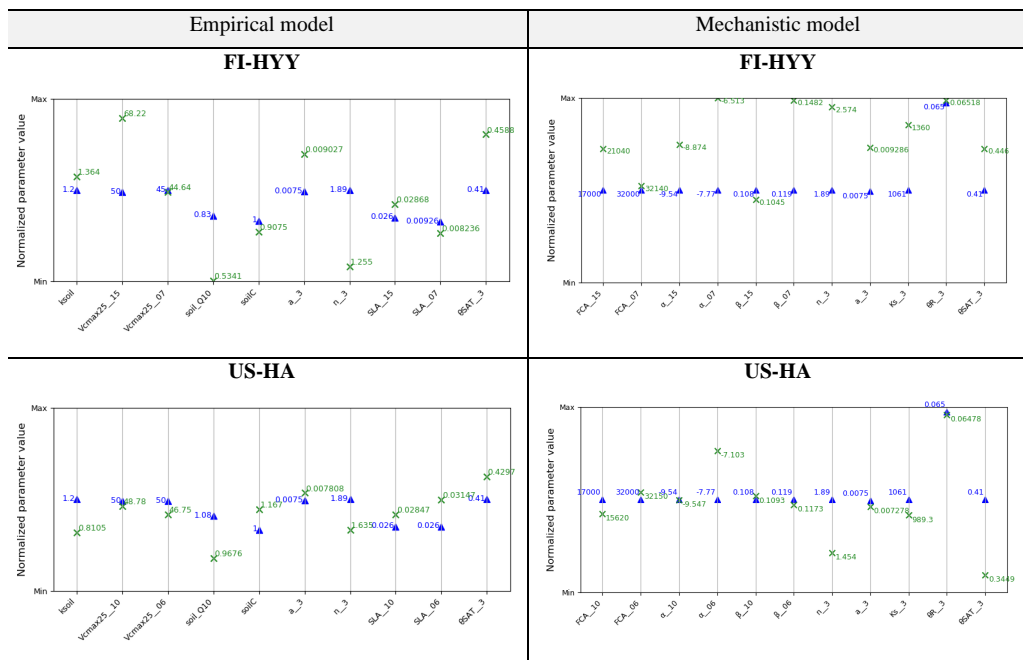
910

911

912



913 **Appendix E: Prior versus post optimization parameter values**



914 **Figure E1: Comparison between prior and posterior optimization parameter values at FI-HYY and US-HA. The y-axis**
 915 **represents the normalization between the edges of the range of variation for each parameter.**



916 *Code availability.* The CMIP6 version of the ORCHIDEE model including the soil COS sub-models is available
917 on request to the authors. The LMDZ model is available from <http://web.lmd.jussieu.fr/LMDZ/LMDZ6/> (last
918 access: 21 October 2021) under the CeCILL v2 Free Software License.

919

920 *Data availability.* For FI-HYY, we used the 2015 soil chamber COS measurements published in Sun et al. (2018).
921 For US-HA, we used the soil COS flux data derived from eddy covariance COS and CO₂ measurements and soil
922 chamber CO₂ measurements conducted in 2012 and 2013, published in Wehr et al. (2017). We used the COS flux
923 data published in Kitz et al. (2020) and Spielmann et al. (2019) for AT-NEU in 2015, DK-SOR and ES-LMA in
924 2016 and IT-CRO in 2017.

925

926 *Author contributions.* CA, FM, MR, and PP conceived the research. JO advised regarding the spatialization of his
927 mechanistic model. CA and FM coded the ORCHIDEE developments and made the simulations. MR transported
928 all COS sinks and sources with the LMDZ model. FK, FMS, and GW provided the data for AT-NEU, ES-LMA,
929 DK-SOR, IT-CRO and ET-JA. WS provided the data for FI-HYY site and RW for the US-HA site. NR provided
930 code and guidance for the sensitivity analysis and data assimilation experiments. SB, JEC, MEW, DH, STL, US
931 and DM were consulted on their respective expertise.

932

933 *Competing interests.* The authors declare that they have no conflict of interest.

934

935 *Acknowledgments.*

936 The authors are very grateful to everyone who participated in field data collection used in this study. We thank
937 Vladislav Bastrikov for providing the ORCHIDAS code. We also acknowledge Nicolas Vuichard for providing
938 the soil bulk density map used in ORCHIDEE simulations. Operation of the US-HA site is supported by the
939 AmeriFlux Management Project with funding by the U.S. Department of Energy's Office of Science under
940 Contract No. DE-AC02-05CH11231 and additionally is a part of the Harvard Forest LTER site supported by the
941 National Science Foundation (DEB-1832210). The field campaign at DK-SOR was supported by the Danish ICOS
942 contribution (ICOS/DK) and by the Danish Council for Independent Research grant DFF-1323-00182.

943

944 *Financial support.*

945 This research has been mainly supported by the European Commission, Horizon 2020 Framework Programme,
946 4C (grant no. 821003) and to a small extend VERIFY (grant no. 776810)

947 FK, FMS and GW acknowledge funding by the Austrian National Science Fund (FWF) through contracts P26931,
948 P27176, P31669 and I03859 and the University of Innsbruck.

949



950 References

951

952 Aneja, V. P., Overton, J. H., and Aneja, A. P.: Emission survey of biogenic sulfur flux from terrestrial surfaces,
953 31, 256–258, <https://doi.org/10.1080/00022470.1981.10465218>, 1981.

954 Barba, J., Cueva, A., Bahn, M., Barron-Gafford, G. A., Bond-Lamberty, B., Hanson, P. J., Jaimes, A., Kulmala,
955 L., Pumpanen, J., Scott, R. L., Wohlfahrt, G., and Vargas, R.: Comparing ecosystem and soil respiration: review
956 and key challenges of tower-based and soil measurements, 2018.

957 Bastrikov, V., Macbean, N., Bacour, C., Santaren, D., Kuppel, S., and Peylin, P.: Land surface model parameter
958 optimisation using in situ flux data: Comparison of gradient-based versus random search algorithms (a case study
959 using ORCHIDEE v1.9.5.2), 11, 4739–4754, <https://doi.org/10.5194/gmd-11-4739-2018>, 2018.

960 Belviso, S., Schmidt, M., Yver, C., Ramonet, M., Gros, V., and Launois, T.: Strong similarities between night-
961 time deposition velocities of carbonyl sulphide and molecular hydrogen inferred from semi-continuous
962 atmospheric observations in Gif-sur-Yvette, Paris region, 65, 20719, <https://doi.org/10.3402/tellusb.v65i0.20719>,
963 2013.

964 Belviso, S., Lebegue, B., Ramonet, M., Kazan, V., Pison, I., Berchet, A., Delmotte, M., Yver-Kwok, C., Montagne,
965 D., and Ciais, P.: A top-down approach of sources and non-photosynthetic sinks of carbonyl sulfide from
966 atmospheric measurements over multiple years in the Paris region (France),
967 <https://doi.org/10.1371/journal.pone.0228419i>, 2020.

968 Berkelhammer, M., Asaf, D., Still, C., Montzka, S., Noone, D., Gupta, M., Provencal, R., Chen, H., and Yakir, D.:
969 Constraining surface carbon fluxes using in situ measurements of carbonyl sulfide and carbon dioxide, 28, 161–
970 179, <https://doi.org/10.1002/2013GB004644>, 2014.

971 Berry, J., Wolf, A., Campbell, J. E., Baker, I., Blake, N., Blake, D., Denning, A. S., Kawa, S. R., Montzka, S. A.,
972 Seibt, U., Stimler, K., Yakir, D., and Zhu, Z.: A coupled model of the global cycles of carbonyl sulfide and CO₂:
973 A possible new window on the carbon cycle, 118, 842–852, <https://doi.org/10.1002/jgrg.20068>, 2013.

974 Bird, B., Stewart, W., and Lightfoot, E.: *Transport Phenomena*, 2002.

975 Boucher, O., Servonnat, J., Albright, A. L., Aumont, O., Balkanski, Y., Bastrikov, V., Bekki, S., Bonnet, R., Bony,
976 S., Bopp, L., Braconnot, P., Brockmann, P., Cadule, P., Caubel, A., Cheruy, F., Codron, F., Cozic, A., Cugnet, D.,
977 D’Andrea, F., Davini, P., de Lavergne, C., Denvil, S., Deshayes, J., Devilliers, M., Ducharme, A., Dufresne, J. L.,
978 Dupont, E., Éthé, C., Fairhead, L., Falletti, L., Flavoni, S., Foujols, M. A., Gardoll, S., Gastineau, G., Ghattas, J.,
979 Grandpeix, J. Y., Guenet, B., Guez, L. E., Guilyardi, E., Guimberteau, M., Hauglustaine, D., Hourdin, F., Idelkadi,
980 A., Joussaume, S., Kageyama, M., Khodri, M., Krinner, G., Lebas, N., Levvasseur, G., Lévy, C., Li, L., Lott, F.,
981 Lurton, T., Luyssaert, S., Madec, G., Madeleine, J. B., Maignan, F., Marchand, M., Marti, O., Mellul, L.,
982 Meurdesoif, Y., Mignot, J., Musat, I., Ottlé, C., Peylin, P., Planton, Y., Polcher, J., Rio, C., Rochetin, N., Rousset,
983 C., Sepulchre, P., Sima, A., Swingedouw, D., Thiéblemont, R., Traore, A. K., Vancoppenolle, M., Vial, J., Vialard,
984 J., Viovy, N., and Vuichard, N.: Presentation and Evaluation of the IPSL-CM6A-LR Climate Model, 12,
985 <https://doi.org/10.1029/2019MS002010>, 2020.

986 Brændholt, A., Ibrom, A., Larsen, K. S., and Pilegaard, K.: Partitioning of ecosystem respiration in a beech forest,
987 252, 88–98, <https://doi.org/10.1016/j.agrformet.2018.01.012>, 2018.

988 Burkholder, J. B., Sander, S. P., Abbatt, J. P. D., Barker, J. R., Cappa, C., Crounse, J. D., Dibble, T. S., Huie, R.
989 E., Kolb, C. E., Kurylo, M. J., Orkin, V. L., Percival, C. J., Wilmouth, D. M., and Wine, P. H.: Chemical Kinetics



- 990 and Photochemical Data for Use in Atmospheric Studies Evaluation Number 19 NASA Panel for Data Evaluation,
991 2019.
- 992 Campbell, J. E., Carmichael, G. R., Chai, T., Mena-Carrasco, M., Tang, Y., Blake, D. R., Blake, N. J., Vay, S. A.,
993 Collatz, G. J., Baker, I., Berry, J. A., Montzka, S. A., Sweeney, C., Schnoor, J. L., and Stanier, C. O.:
994 Photosynthetic control of atmospheric carbonyl sulfide during the growing season, 322, 1085–1088,
995 <https://doi.org/10.1126/science.1164015>, 2008.
- 996 Campolongo, F., Cariboni, J., and Saltelli, A.: An effective screening design for sensitivity analysis of large
997 models, 22, 1509–1518, <https://doi.org/10.1016/j.envsoft.2006.10.004>, 2007.
- 998 Cheruy, F., Ducharne, A., Hourdin, F., Musat, I., Vignon, É., Gastineau, G., Bastrikov, V., Vuichard, N., Diallo,
999 B., Dufresne, J. L., Ghattas, J., Grandpeix, J. Y., Idelkadi, A., Mellul, L., Maignan, F., Ménégoz, M., Ottlé, C.,
1000 Peylin, P., Servonnat, J., Wang, F., and Zhao, Y.: Improved Near-Surface Continental Climate in IPSL-CM6A-
1001 LR by Combined Evolutions of Atmospheric and Land Surface Physics, 12,
1002 <https://doi.org/10.1029/2019MS002005>, 2020.
- 1003 Chin, M. and Davis, D. D.: A reanalysis of carbonyl sulfide as a source of stratospheric background sulfur aerosol,
1004 100, 8993–9005, <https://doi.org/10.1029/95JD00275>, 1995.
- 1005 Dantec-Nédélec, S., Ottlé, C., Wang, T., Guglielmo, F., Maignan, F., Delbart, N., Valdayskikh, V., Radchenko,
1006 T., Nekrasova, O., Zakharov, V., and Jouzel, J.: Testing the capability of ORCHIDEE land surface model to
1007 simulate Arctic ecosystems: Sensitivity analysis and site-level model calibration, 9, 1212–1230,
1008 <https://doi.org/10.1002/2016MS000860>, 2017.
- 1009 Davidson, C., Amrani, A., and Angert, A.: Tropospheric carbonyl sulfide mass balance based on direct
1010 measurements of sulfur isotopes, <https://doi.org/10.1073/pnas.2020060118/-/DCSupplemental>, 2021.
- 1011 Deepagoda, T. K. K. C., Moldrup, P., Schjønning, P., de Jonge, L. W., Kawamoto, K., and Komatsu, T.: Density-
1012 Corrected Models for Gas Diffusivity and Air Permeability in Unsaturated Soil, 10, 226–238, <https://doi.org/10.2136/vzj2009.0137>, 2011.
- 1014 Devai, I. and DeLaune, R. D.: Trapping Efficiency of Various Solid Adsorbents for Sampling and Quantitative
1015 Gas Chromatographic Analysis of Carbonyl Sulfide, 30, 187–198, <https://doi.org/10.1080/00032719708002300>,
1016 1997.
- 1017 van Diest, H. and Kesselmeier, J.: Soil atmosphere exchange of carbonyl sulfide (COS) regulated by diffusivity
1018 depending on water-filled pore space, *Biogeosciences*, 475–483 pp., 2008.
- 1019 Elliott, S., Lu, E., and Rowland, F. S.: Rates and mechanisms for the hydrolysis of carbonyl sulfide in natural
1020 waters, 23, 458–461, <https://doi.org/10.1021/es00181a011>, 1989.
- 1021 El-Madany, T. S., Reichstein, M., Perez-Priego, O., Carrara, A., Moreno, G., Pilar Martín, M., Pacheco-Labrador,
1022 J., Wohlfahrt, G., Nieto, H., Weber, U., Kolle, O., Luo, Y. P., Carvalhais, N., and Migliavacca, M.: Drivers of
1023 spatio-temporal variability of carbon dioxide and energy fluxes in a Mediterranean savanna ecosystem, 262, 258–
1024 278, <https://doi.org/10.1016/j.agrformet.2018.07.010>, 2018.
- 1025 Folberth, G. A., Hauglustaine, D. A., Lathèrre, J., and Brocheton, F.: Interactive chemistry in the Laboratoire de
1026 Météorologie Dynamique general circulation model: model description and impact analysis of biogenic
1027 hydrocarbons on tropospheric chemistry, *Atmos. Chem. Phys.*, 2273–2319 pp., 2006.
- 1028 Friedlingstein, P., O’Sullivan, M., Jones, M. W., Andrew, R. M., Hauck, J., Olsen, A., Peters, G. P., Peters, W.,
1029 Pongratz, J., Sitch, S., le Quéré, C., Canadell, J. G., Ciais, P., Jackson, R. B., Alin, S., Aragão, L. E. O. C., Armeth,



- 1030 A., Arora, V., Bates, N. R., Becker, M., Benoit-Cattin, A., Bittig, H. C., Bopp, L., Bultan, S., Chandra, N.,
1031 Chevallier, F., Chini, L. P., Evans, W., Florentie, L., Forster, P. M., Gasser, T., Gehlen, M., Gilfillan, D., Gkritzalis,
1032 T., Gregor, L., Gruber, N., Harris, I., Hartung, K., Haverd, V., Houghton, R. A., Ilyina, T., Jain, A. K., Joetzjer,
1033 E., Kadono, K., Kato, E., Kitidis, V., Korsbakken, J. I., Landschützer, P., Lefèvre, N., Lenton, A., Lienert, S., Liu,
1034 Z., Lombardozi, D., Marland, G., Metzl, N., Munro, D. R., Nabel, J. E. M. S., Nakaoka, S. I., Niwa, Y., O'Brien,
1035 K., Ono, T., Palmer, P. I., Pierrot, D., Poulter, B., Resplandy, L., Robertson, E., Rödenbeck, C., Schwinger, J.,
1036 Séférian, R., Skjelvan, I., Smith, A. J. P., Sutton, A. J., Tanhua, T., Tans, P. P., Tian, H., Tilbrook, B., van der
1037 Werf, G., Vuichard, N., Walker, A. P., Wanninkhof, R., Watson, A. J., Willis, D., Wiltshire, A. J., Yuan, W., Yue,
1038 X., and Zaehle, S.: Global Carbon Budget 2020, 12, 3269–3340, <https://doi.org/10.5194/essd-12-3269-2020>, 2020.
1039 van Genuchten, M. Th.: A closed-form equation for predicting the hydraulic conductivity of unsaturated soils,
1040 44(5), 892–898, 1980.
- 1041 Giasson, M. A., Ellison, A. M., Bowden, R. D., Crill, P. M., Davidson, E. A., Drake, J. E., Frey, S. D., Hadley, J.
1042 L., Lavine, M., Melillo, J. M., Munger, J. W., Nadelhoffer, K. J., Nicoll, L., Ollinger, S. v., Savage, K. E., Steudler,
1043 P. A., Tang, J., Varner, R. K., Wofsy, S. C., Foster, D. R., and Finzi, A. C.: Soil respiration in a northeastern US
1044 temperate forest: A 22-year synthesis, 4, <https://doi.org/10.1890/ES13.00183.1>, 2013.
- 1045 Glatthor, N., Höpfner, M., Baker, I. T., Berry, J., Campbell, J. E., Kawa, S. R., Krysztofiak, G., Leysner, A.,
1046 Sinnhuber, B. M., Stiller, G. P., Stinecipher, J., and von Clarmann, T.: Tropical sources and sinks of carbonyl
1047 sulfide observed from space, 42, 10082–10090, <https://doi.org/10.1002/2015GL066293>, 2015.
- 1048 Goldberg, D. E.: Genetic Algorithms in Search, Optimization, and Machine Learning., 1989.
- 1049 Hauglustaine, D. A., Hourdin, F., Jourdain, L., Filiberti, M. A., Walters, S., Lamarque, J. F., and Holland, E. A.:
1050 Interactive chemistry in the Laboratoire de Météorologie Dynamique general circulation model: Description and
1051 background tropospheric chemistry evaluation, 109, <https://doi.org/10.1029/2003jd003957>, 2004.
- 1052 Hauglustaine, D. A., Balkanski, Y., and Schulz, M.: A global model simulation of present and future nitrate
1053 aerosols and their direct radiative forcing of climate, 14, 11031–11063, [https://doi.org/10.5194/acp-14-11031-](https://doi.org/10.5194/acp-14-11031-2014)
1054 2014, 2014.
- 1055 Haupt, R. L. and Haupt, S. E.: Practical Genetic Algorithms., Wiley., 2004.
- 1056 Hersbach, H., Bell, B., Berrisford, P., Hirahara, S., Horányi, A., Muñoz-Sabater, J., Nicolas, J., Peubey, C., Radu,
1057 R., Schepers, D., Simmons, A., Soci, C., Abdalla, S., Abellan, X., Balsamo, G., Bechtold, P., Biavati, G., Bidlot,
1058 J., Bonavita, M., de Chiara, G., Dahlgren, P., Dee, D., Diamantakis, M., Dragani, R., Flemming, J., Forbes, R.,
1059 Fuentes, M., Geer, A., Haimberger, L., Healy, S., Hogan, R. J., Hólm, E., Janisková, M., Keeley, S., Laloyaux, P.,
1060 Lopez, P., Lupu, C., Radnoti, G., de Rosnay, P., Rozum, I., Vamborg, F., Villaume, S., and Thépaut, J. N.: The
1061 ERA5 global reanalysis, 146, 1999–2049, <https://doi.org/10.1002/qj.3803>, 2020.
- 1062 Hörtnagl, L., Bamberger, I., Graus, M., Ruuskanen, T. M., Schnitzhofer, R., Müller, M., Hansel, A., and
1063 Wohlfahrt, G.: Biotic, abiotic, and management controls on methanol exchange above a temperate mountain
1064 grassland, 116, <https://doi.org/10.1029/2011JG001641>, 2011.
- 1065 Hörtnagl, L. and Wohlfahrt, G.: Methane and nitrous oxide exchange over a managed hay meadow, 11, 7219–
1066 7236, <https://doi.org/10.5194/bg-11-7219-2014>, 2014.
- 1067 Hourdin, F. and Issartel, J. P.: Sub-surface nuclear tests monitoring through the CTBT xenon network, 27, 2245–
1068 2248, <https://doi.org/10.1029/1999GL010909>, 2000.



- 1069 Hourdin, F., Rio, C., Grandpeix, J. Y., Madeleine, J. B., Cheruy, F., Rochetin, N., Jam, A., Musat, I., Idelkadi, A.,
1070 Fairhead, L., Foujols, M. A., Mellul, L., Traore, A. K., Dufresne, J. L., Boucher, O., Lefebvre, M. P., Millour, E.,
1071 Vignon, E., Jouhaud, J., Diallo, F. B., Lott, F., Gastineau, G., Caubel, A., Meurdesoif, Y., and Ghattas, J.:
1072 LMDZ6A: The Atmospheric Component of the IPSL Climate Model With Improved and Better Tuned Physics,
1073 12, <https://doi.org/10.1029/2019MS001892>, 2020.
- 1074 Kanda, K. I., Tsuruta, H., and Minami, K.: Emission of dimethyl sulfide, carbonyl sulfide, and carbon bisulfide
1075 from paddy fields, 38, 709–716, <https://doi.org/10.1080/00380768.1992.10416701>, 1992.
- 1076 Kesselmeier, J., Teusch, N., and Kuhn, U.: Controlling variables for the uptake of atmospheric carbonyl sulfide
1077 by soil, 104, 11577–11584, <https://doi.org/10.1029/1999JD900090>, 1999.
- 1078 Kettle, A. J., Kuhn, U., von Hobe, M., Kesselmeier, J., and Andreae, M. O.: Global budget of atmospheric carbonyl
1079 sulfide: Temporal and spatial variations of the dominant sources and sinks, 107,
1080 <https://doi.org/10.1029/2002JD002187>, 2002.
- 1081 Kitz, F., Gerdel, K., Hammerle, A., Laterza, T., Spielmann, F. M., and Wohlfahrt, G.: In situ soil COS exchange
1082 of a temperate mountain grassland under simulated drought, 183, 851–860, [https://doi.org/10.1007/s00442-016-](https://doi.org/10.1007/s00442-016-3805-0)
1083 3805-0, 2017.
- 1084 Kitz, F., Spielmann, F. M., Hammerle, A., Kolle, O., Migliavacca, M., Moreno, G., Ibrom, A., Krasnov, D., Noe,
1085 S. M., and Wohlfahrt, G.: Soil COS Exchange: A Comparison of Three European Ecosystems, 34,
1086 <https://doi.org/10.1029/2019GB006202> (last access: 21 Octobre 2021), 2020.
- 1087 Kolari, P., Kulmala, L., Pumpanen, J., Launiainen, S., Ilvesniemi, H., Hari, P., and Nikinmaa, E.: CO₂ exchange
1088 and component CO₂ fluxes of a boreal Scots pine forest, 2009.
- 1089 Kooijmans, L. M. J., Cho, A., Ma, J., Kaushik, A., Haynes, K. D., Baker, I., Lujikx, I. T., Groenink, M., Peters,
1090 W., Miller, J., Berry, J. A., Ogée, J., Meredith, L. K., Sun, W., -Maaria, K., Krol, M., and Kooijmans, L.:
1091 Evaluation of carbonyl sulfide biosphere exchange in the Simple Biosphere Model (SiB4), 10, 20,
1092 <https://doi.org/10.5194/bg-2021-192>, 2021.
- 1093 Kuai, L., Worden, J. R., Campbell, J. E., Kulawik, S. S., Li, K. F., Lee, M., Weidner, R. J., Montzka, S. A., Moore,
1094 F. L., Berry, J. A., Baker, I., Denning, A. S., Bian, H., Bowman, K. W., Liu, J., and Yung, Y. L.: Estimate of
1095 carbonyl sulfide tropical oceanic surface fluxes using aura tropospheric emission spectrometer observations, 120,
1096 11,012–11,023, <https://doi.org/10.1002/2015JD023493>, 2015.
- 1097 Kuppel, S., Peylin, P., Maignan, F., Chevallier, F., Kiely, G., Montagnani, L., and Cescatti, A.: Model-data fusion
1098 across ecosystems: From multisite optimizations to global simulations, 7, 2581–2597,
1099 <https://doi.org/10.5194/gmd-7-2581-2014>, 2014.
- 1100 Lardy, R., Bellocchi, G., and Soussana, J. F.: A new method to determine soil organic carbon equilibrium, 26,
1101 1759–1763, <https://doi.org/10.1016/j.envsoft.2011.05.016>, 2011.
- 1102 Launois, T., Peylin, P., Belviso, S., and Poulter, B.: A new model of the global biogeochemical cycle of carbonyl
1103 sulfide - Part 2: Use of carbonyl sulfide to constrain gross primary productivity in current vegetation models, 15,
1104 9285–9312, <https://doi.org/10.5194/acp-15-9285-2015>, 2015.
- 1105 Lennartz, S. T., Marandino, C. A., von Hobe, M., Cortes, P., Quack, B., Simo, R., Booge, D., Pozzer, A., Steinhoff,
1106 T., Arevalo-Martinez, D. L., Kloss, C., Bracher, A., Atlas, E., and Krüger, K.: Direct oceanic emissions unlikely
1107 to account for the missing source of atmospheric carbonyl sulfide, 17, 385–402, [https://doi.org/10.5194/acp-17-](https://doi.org/10.5194/acp-17-385-2017)
1108 385-2017, 2017.



- 1109 Lennartz, S., A Marandino, C., von Hobe, M., O Andreae, M., Aranami, K., Atlas, E., Berkelhammer, M.,
1110 Bingemer, H., Booge, D., Cutter, G., Cortes, P., Kremser, S., S Law, C., Marriner, A., Simó, R., Quack, B., Xie,
1111 H., and Xu, X.: Marine carbonyl sulfide (OCS) and carbon disulfide (CS₂): A compilation of measurements in
1112 seawater and the marine boundary layer, 12, 591–609, <https://doi.org/10.5194/essd-12-591-2020>, 2020.
- 1113 Lennartz, S. T., Gauss, M., von Hobe, M., and Marandino, C. A.: Monthly resolved modelled oceanic emissions
1114 of carbonyl sulphide and carbon disulphide for the period 2000–2019, 13, 2095–2110,
1115 <https://doi.org/10.5194/essd-13-2095-2021>, 2021.
- 1116 Liu, J., Geng, C., Mu, Y., Zhang, Y., Xu, Z., and Wu, H.: Exchange of carbonyl sulfide (COS) between the
1117 atmosphere and various soils in China, *Biogeosciences*, 753–762 pp., 2010.
- 1118 Lopez-Sangil, L., Rousk, J., Wallander, H., and Casals, P.: Microbial growth rate measurements reveal that land-
1119 use abandonment promotes a fungal dominance of SOM decomposition in grazed Mediterranean ecosystems, 47,
1120 129–138, <https://doi.org/10.1007/s00374-010-0510-8>, 2011.
- 1121 Ma, X., Huang, J., Zhao, T., Liu, C., Zhao, K., Xing, J., and Xiao, W.: Rapid increase in summer surface ozone
1122 over the North China Plain during 2013–2019: A side effect of particulate matter reduction control?, 21, 1–16,
1123 <https://doi.org/10.5194/acp-21-1-2021>, 2021.
- 1124 MacBean, N., Maignan, F., Bacour, C., Lewis, P., Peylin, P., Guanter, L., Köhler, P., Gómez-Dans, J., and Disney,
1125 M.: Strong constraint on modelled global carbon uptake using solar-induced chlorophyll fluorescence data, 8,
1126 <https://doi.org/10.1038/s41598-018-20024-w>, 2018.
- 1127 Mahmud, K., Scott, R. L., Biederman, J. A., Litvak, M. E., Kolb, T., Meyers, T. P., Bastrikov, V., and MacBean,
1128 N.: Optimizing Carbon Cycle Parameters Drastically Improves Terrestrial Biosphere Model Underestimates of
1129 Dryland Mean Net CO₂ Flux and its Inter-Annual Variability, 2021.
- 1130 Maignan, F., Abadie, C., Remaud, M., Kooijmans, L. M. J., Kohonen, K.-M., Commane, R., Wehr, R., Campbell,
1131 J. E., Belviso, S., Montzka, S. A., Raoult, N., Seibt, U., Shiga, Y. P., Vuichard, N., Whelan, M. E., and Peylin, P.:
1132 Carbonyl sulfide: comparing a mechanistic representation of the vegetation uptake in a land surface model and the
1133 leaf relative uptake approach, 18, 2917–2955, <https://doi.org/10.5194/bg-18-2917-2021>, 2021.
- 1134 Masaki, Y., Iizuka, R., Kato, H., Kojima, Y., Ogawa, T., Yoshida, M., Matsushita, Y., and Katayama, Y.: Fungal
1135 carbonyl sulfide hydrolase of trichoderma harzianum strain thif8 and its relationship with clade D β-carbonic
1136 anhydrases, 36, <https://doi.org/10.1264/jsme2.ME20058>, 2021.
- 1137 Maseyk, K., Berry, J. A., Billesbach, D., Campbell, J. E., Torn, M. S., Zahniser, M., and Seibt, U.: Sources and
1138 sinks of carbonyl sulfide in an agricultural field in the Southern Great Plains, 111, 9064–9069,
1139 <https://doi.org/10.1073/pnas.1319132111>, 2014.
- 1140 Masotti, I., Belviso, S., Bopp, L., Tagliabue, A., and Bucciarelli, E.: Effects of light and phosphorus on summer
1141 DMS dynamics in subtropical waters using a global ocean biogeochemical model, in: *Environmental Chemistry*,
1142 379–389, <https://doi.org/10.1071/EN14265>, 2016.
- 1143 Massman, W. J.: A review of the molecular diffusivities of H and NO in air, O and N near STP, *Atmospheric*
1144 *Environment*, 1111–1127 pp., 1998.
- 1145 Mellillo, J. M. and Steudler, P. A.: The effect of nitrogen fertilization on the COS and CS₂ emissions from
1146 temperature forest soils, 9, 411–417, <https://doi.org/10.1007/BF00114753>, 1989.



- 1147 de Mello, W. Z. and Hines, M. E.: Application of static and dynamic enclosures for determining dimethyl sulfide
1148 and carbonyl sulfide exchange in Sphagnum peatlands: Implications for the magnitude and direction of flux,
1149 JOURNAL OF GEOPHYSICAL RESEARCH, 601–615 pp., 1994.
- 1150 Meredith, L. K., Boye, K., Youngerman, C., Whelan, M., Ogée, J., Sauze, J., and Wingate, L.: Coupled biological
1151 and abiotic mechanisms driving carbonyl sulfide production in soils, 2, 1–27,
1152 <https://doi.org/10.3390/soilsystems2030037>, 2018.
- 1153 Meredith, L. K., Ogée, J., Boye, K., Singer, E., Wingate, L., von Sperber, C., Sengupta, A., Whelan, M., Pang, E.,
1154 Keiluweit, M., Brüggemann, N., Berry, J. A., and Welander, P. v.: Soil exchange rates of COS and CO¹⁸O differ
1155 with the diversity of microbial communities and their carbonic anhydrase enzymes, 13, 290–300,
1156 <https://doi.org/10.1038/s41396-018-0270-2>, 2019.
- 1157 Millington, R. J. and Quirk, J. P.: Permeability of porous solids, 57, 1200–1207,
1158 <https://doi.org/10.1039/TF9615701200>, 1961.
- 1159 Moldrup, P., Olesen, T., Komatsu, T., Yoshikawa, S., Schjønning, P., and Rolston, D. E.: Modeling diffusion and
1160 reaction in soils: x. a unifying model for solute and gas diffusivity in unsaturated soil, 168, 2003.
- 1161 Montzka, S. A., Calvert, P., Hall, B. D., Elkins, J. W., Conway, T. J., Tans, P. P., and Sweeney, C. S.: On the
1162 global distribution, seasonality, and budget of atmospheric carbonyl sulfide (COS) and some similarities to CO₂,
1163 112, <https://doi.org/10.1029/2006JD007665>, 2007.
- 1164 Morris, M. D.: Factorial Sampling Plans for Preliminary Computational Experiments, 33, 161–174,
1165 <https://doi.org/10.1080/00401706.1991.10484804>, 1991.
- 1166 Noe, S. M., Kimmel, V., Hüve, K., Copolovici, L., Portillo-Estrada, M., Püttsepp, Ü., Jõgiste, K., Niinemets, Ü.,
1167 Hörtnagl, L., and Wohlfahrt, G.: Ecosystem-scale biosphere-atmosphere interactions of a hemiboreal mixed forest
1168 stand at Järvselja, Estonia, 262, 71–81, <https://doi.org/10.1016/j.foreco.2010.09.013>, 2011.
- 1169 Noe, S. M., Niinemets, Ü., Krasnova, A., Krasnov, D., Motallebi, A., Kängsepp, V., Jõgiste, K., Hörrak, U.,
1170 Komsaare, K., Mirmo, S., Vana, M., Tammet, H., Bäck, J., Vesala, T., Kulmala, M., Petäjä, T., and Kangur, A.:
1171 SMEAR Estonia: Perspectives of a large-scale forest ecosystem– Atmosphere research infrastructure, 63, 56–84,
1172 <https://doi.org/10.1515/fsmu-2015-0009>, 2015.
- 1173 Ogée, J., Sauze, J., Kesselmeier, J., Genty, B., van Diest, H., Launois, T., and Wingate, L.: A new mechanistic
1174 framework to predict OCS fluxes from soils, 13, 2221–2240, <https://doi.org/10.5194/bg-13-2221-2016>, 2016.
- 1175 Parazoo, N. C., Denning, A. S., Berry, J. A., Wolf, A., Randall, D. A., Kawa, S. R., Pauluis, O., and Doney, S. C.:
1176 Moist synoptic transport of CO₂ along the mid-latitude storm track, 38, <https://doi.org/10.1029/2011GL047238>,
1177 2011.
- 1178 Pastorello, G., Trotta, C., Canfora, E., Chu, H., Christianson, D., Cheah, Y. W., Poindexter, C., Chen, J.,
1179 Elbashandy, A., Humphrey, M., Isaac, P., Polidori, D., Ribeca, A., van Ingen, C., Zhang, L., Amiro, B., Ammann,
1180 C., Arain, M. A., Ardö, J., Arkebauer, T., Arndt, S. K., Arriga, N., Aubinet, M., Aurela, M., Baldocchi, D., Barr,
1181 A., Beamesderfer, E., Marchesini, L. B., Bergeron, O., Beringer, J., Bernhofer, C., Berveiller, D., Billesbach, D.,
1182 Black, T. A., Blanken, P. D., Bohrer, G., Boike, J., Bolstad, P. v., Bonal, D., Bonnefond, J. M., Bowling, D. R.,
1183 Bracho, R., Brodeur, J., Brümmer, C., Buchmann, N., Burban, B., Burns, S. P., Buysse, P., Cale, P., Cavagna, M.,
1184 Cellier, P., Chen, S., Chini, I., Christensen, T. R., Cleverly, J., Collalti, A., Consalvo, C., Cook, B. D., Cook, D.,
1185 Coursolle, C., Cremonese, E., Curtis, P. S., D’Andrea, E., da Rocha, H., Dai, X., Davis, K. J., de Cinti, B., de
1186 Grandcourt, A., de Ligne, A., de Oliveira, R. C., Delpierre, N., Desai, A. R., di Bella, C. M., di Tommasi, P.,



- 1187 Dolman, H., Domingo, F., Dong, G., Dore, S., Duce, P., Dufrêne, E., Dunn, A., Dušek, J., Eamus, D., Eichelmann,
1188 U., ElKhidir, H. A. M., Eugster, W., Ewenz, C. M., Ewers, B., Famulari, D., Fares, S., Feigenwinter, I., Feitz, A.,
1189 Fensholt, R., Filippa, G., Fischer, M., Frank, J., Galvagno, M., Gharun, M., Gianelle, D., et al.: The
1190 FLUXNET2015 dataset and the ONEFlux processing pipeline for eddy covariance data, 7, 225,
1191 <https://doi.org/10.1038/s41597-020-0534-3>, 2020.
- 1192 Peylin, P., Ciais, P., Denning, A. S., Tans, P. P., Berry, J. A., and White, J. W. C.: A 3-dimensional study of δ^{18}
1193 O in atmospheric CO₂: contribution of different land ecosystems, 51, 642–667,
1194 <https://doi.org/10.3402/tellusb.v51i3.16452>, 1999.
- 1195 Peylin, P., Bacour, C., MacBean, N., Leonard, S., Rayner, P., Kuppel, S., Koffi, E., Kane, A., Maignan, F.,
1196 Chevallier, F., Ciais, P., and Prunet, P.: A new stepwise carbon cycle data assimilation system using multiple data
1197 streams to constrain the simulated land surface carbon cycle, 9, 3321–3346, [https://doi.org/10.5194/gmd-9-3321-](https://doi.org/10.5194/gmd-9-3321-2016)
1198 2016, 2016.
- 1199 Pilegaard, K., Ibrom, A., Courtney, M. S., Hummelshøj, P., and Jensen, N. O.: Increasing net CO₂ uptake by a
1200 Danish beech forest during the period from 1996 to 2009, 151, 934–946,
1201 <https://doi.org/10.1016/j.agrformet.2011.02.013>, 2011.
- 1202 Protoschill-Krebs, G., Wilhelm, C., and Kesselmeier, J.: Consumption of carbonyl sulphide (COS) by higher plant
1203 carbonic anhydrase (CA), *Atmospheric Environment*, 996 pp., 1996.
- 1204 Raoult, N., Ottlé, C., Peylin, P., Bastrikov, V., and Maugis, P.: Evaluating and Optimizing Surface Soil Moisture
1205 Drydowns in the ORCHIDEE Land Surface Model at In Situ Locations, <https://doi.org/10.1175/JHM-D-20, 2021>.
- 1206 Remaud, M., Chevallier, F., Cozic, A., Lin, X., and Bousquet, P.: On the impact of recent developments of the
1207 LMDz atmospheric general circulation model on the simulation of CO₂ transport, 11, 4489–4513,
1208 <https://doi.org/10.5194/gmd-11-4489-2018>, 2018.
- 1209 Remaud, M., Chevallier, F., Maignan, F., Belviso, S., Berchet, A., Parouffe, A., Abadie, C., Bacour, C., Lennartz,
1210 S., and Peylin, P.: Plant gross primary production, plant respiration and carbonyl sulfide emissions over the globe
1211 inferred by atmospheric inverse modelling, <https://doi.org/10.5194/acp-2021-326>, 2021.
- 1212 Reynolds, C. A., Jackson, T. J., and Rawls, W. J.: Estimating soil water-holding capacities by linking the Food
1213 and Agriculture Organization soil map of the world with global pedon databases and continuous pedotransfer
1214 functions, 36, 3653–3662, <https://doi.org/10.1029/2000WR900130>, 2000.
- 1215 Sandoval-Soto, L., Stanimirov, M., von Hobe, M., Schmitt, V., Valdes, J., Wild, A., and Kesselmeier, J.: Global
1216 uptake of carbonyl sulfide (COS) by terrestrial vegetation: Estimates corrected by deposition velocities normalized
1217 to the uptake of carbon dioxide (CO₂), *Biogeosciences*, 125–132 pp., 2005.
- 1218 Sauze, J., Ogée, J., Maron, P.-A., Crouzet, O., Nowak, V., Wohl, S., Kaisermann, A., Jones, S., Wingate, L., Ee,
1219 O., and Jones, S. P.: The interaction of soil phototrophs and fungi with pH and their impact on soil CO₂, CO¹⁸ O
1220 and OCS exchange, <https://doi.org/10.1016/j.soilbio.2017.09.009>, 2017.
- 1221 Sitch, S., Friedlingstein, P., Gruber, N., Jones, S. D., Murray-Tortarolo, G., Ahlström, A., Doney, S. C., Graven,
1222 H., Heinze, C., Huntingford, C., Levis, S., Levy, P. E., Lomas, M., Poulter, B., Viovy, N., Zaehle, S., Zeng, N.,
1223 Arneeth, A., Bonan, G., Bopp, L., Canadell, J. G., Chevallier, F., Ciais, P., Ellis, R., Gloor, M., Peylin, P., Piao, S.
1224 L., le Quéré, C., Smith, B., Zhu, Z., and Myneni, R.: Recent trends and drivers of regional sources and sinks of
1225 carbon dioxide, 12, 653–679, <https://doi.org/10.5194/bg-12-653-2015>, 2015.



- 1226 Smith, K., Jakubzick, C., Whittam, T., and Ferry, J.: Carbonic anhydrase is an ancient enzyme widespread in
1227 prokaryotes, *P. Natl. Acad. Sci. USA*, 96, 15184–15189, 1999.
- 1228 Smith, K. S. and Ferry, J. G.: Prokaryotic carbonic anhydrases, 24, 335–366, <https://doi.org/10.1111/j.1574->
1229 6976.2000.tb00546.x, 2000.
- 1230 Spielmann, F. M., Wohlfahrt, G., Hammerle, A., Kitz, F., Migliavacca, M., Alberti, G., Ibrom, A., El-Madany, T.
1231 S., Gerdel, K., Moreno, G., Kolle, O., Karl, T., Peressotti, A., and Delle Vedove, G.: Gross Primary Productivity
1232 of Four European Ecosystems Constrained by Joint CO₂ and COS Flux Measurements, 46, 5284–5293,
1233 <https://doi.org/10.1029/2019GL082006> (last access: 21 Octobre 2021), 2019.
- 1234 Spielmann, F., Hammerle, A., Kitz, F., Gerdel, K., and Wohlfahrt, G.: Seasonal dynamics of the COS and CO₂
1235 exchange of a managed temperate grassland, 1–19, <https://doi.org/10.5194/bg-2020-27>, 2020.
- 1236 Stinecipher, J. R., Cameron-Smith, P. J., Blake, N. J., Kuai, L., Lejeune, B., Mahieu, E., Simpson, I. J., and
1237 Campbell, J. E.: Biomass Burning Unlikely to Account for Missing Source of Carbonyl Sulfide, 46, 14912–14920,
1238 <https://doi.org/10.1029/2019GL085567>, 2019.
- 1239 Sun, W., Maseyk, K., Lett, C., and Seibt, U.: A soil diffusion-reaction model for surface COS flux: COSSM v1,
1240 8, 3055–3070, <https://doi.org/10.5194/gmd-8-3055-2015>, 2015.
- 1241 Sun, W., Kooijmans, L. M. J., Maseyk, K., Chen, H., Mammarella, I., Vesala, T., Levula, J., Keskinen, H., and
1242 Seibt, U.: Soil fluxes of carbonyl sulfide (COS), carbon monoxide, and carbon dioxide in a boreal forest in southern
1243 Finland, 18, 1363–1378, <https://doi.org/10.5194/acp-18-1363-2018> (last access: 21 Octobre 2021), 2018.
- 1244 Sweeney, C., Karion, A., Wolter, S., Newberger, T., Guenther, D., Higgs, J. A., Andrews, A. E., Lang, P. M., Neff,
1245 D., Dlugokencky, E., Miller, J. B., Montzka, S. A., Miller, B. R., Masarie, K. A., Biraud, S. C., Novelli, P. C.,
1246 Crotwell, M., Crotwell, A. M., Thoning, K., and Tans, P. P.: Seasonal climatology of CO₂ across north america
1247 from aircraft measurements in the NOAA/ESRL global greenhouse gas reference network, 120, 5155–5190,
1248 <https://doi.org/10.1002/2014JD022591>, 2015.
- 1249 Tarantola, A.: Inverse Problem Theory and Methods for Model Parameter Estimation, Society for Industrial and
1250 Applied Mathematics, <https://doi.org/10.1137/1.9780898717921>, 2005.
- 1251 Terrenoire, E., Hauglustaine, D., Cohen, Y., Cozic, A., Valorso, R., Lefevre, F., Jegou, F., and Matthes, S.: Impact
1252 of present-day and future aircraft NO_x and aerosol emissions on atmospheric composition and associated radiative
1253 forcings of climate, in prep.
- 1254 Thoning, K. W., Tans, P. P., and Komhyr, W. D.: Atmospheric Carbon Dioxide at Mauna Loa Observatory 2.
1255 Analysis of the NOAA GMCC Data, 1974-1985, *JOURNAL OF GEOPHYSICAL RESEARCH*, 8549–8565 pp.,
1256 1989.
- 1257 Tootchi, A., Jost, A., and Ducharne, A.: Multi-source global wetland maps combining surface water imagery and
1258 groundwater constraints, 11, 189–220, <https://doi.org/10.5194/essd-11-189-2019>, 2019.
- 1259 Ulshijfer, V. S., Flijk, O. R., Uher, G., and Andreae, M. O.: Photochemical production and air-sea exchange of
1260 sulfide in the eastern Mediterranean Sea, *Marine Chemistry*, 25–39 pp., 1996.
- 1261 Urbanski, S., Barford, C., Wofsy, S., Kucharik, C., Pyle, E., Budney, J., McKain, K., Fitzjarrald, D., Czikowsky,
1262 M., and Munger, J. W.: Factors controlling CO₂ exchange on timescales from hourly to decadal at Harvard Forest,
1263 112, <https://doi.org/10.1029/2006JG000293>, 2007.
- 1264 Wania, R., Ross, I., and Prentice, I. C.: Implementation and evaluation of a new methane model within a dynamic
1265 global vegetation model: LPJ-WHyMe v1.3.1, 3, 565–584, <https://doi.org/10.5194/gmd-3-565-2010>, 2010.



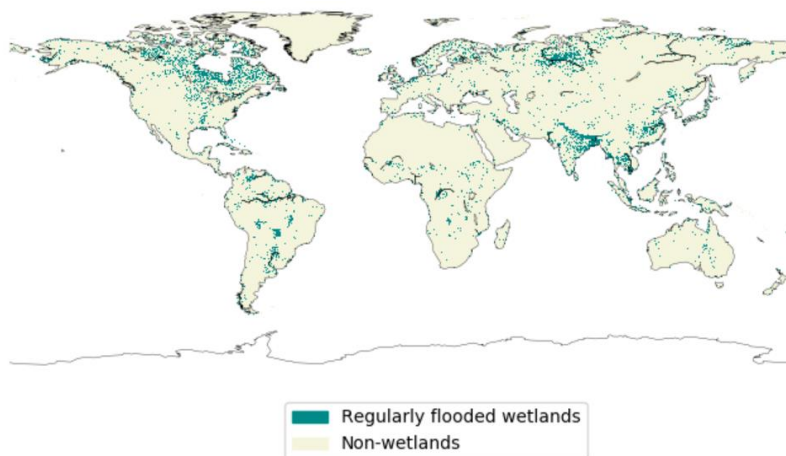
- 1266 Watts, S. F.: The mass budgets of carbonyl sulfide, dimethyl sulfide, carbon disulfide and hydrogen sulfide,
1267 *Atmospheric Environment*, Volume 34, Issue 5, p. 761-779, 2000.
- 1268 Wehr, R., Commane, R., Munger, J. W., Barry Mcmanus, J., Nelson, D. D., Zahniser, M. S., Saleska, S. R., and
1269 Wofsy, S. C.: Dynamics of canopy stomatal conductance, transpiration, and evaporation in a temperate deciduous
1270 forest, validated by carbonyl sulfide uptake, 14, 389–401, <https://doi.org/10.5194/bg-14-389-2017> (last access: 21
1271 Octobre 2021), 2017.
- 1272 Weiner, T., Gross, A., Moreno, G., Migliavacca, M., Schrupf, M., Reichstein, M., Hilman, B., Carrara, A., and
1273 Angert, A.: Following the Turnover of Soil Bioavailable Phosphate in Mediterranean Savanna by Oxygen Stable
1274 Isotopes, 123, 1850–1862, <https://doi.org/10.1029/2017JG004086>, 2018.
- 1275 Whelan, M. E., Min, D. H., and Rhew, R. C.: Salt marsh vegetation as a carbonyl sulfide (COS) source to the
1276 atmosphere, 73, 131–137, <https://doi.org/10.1016/j.atmosenv.2013.02.048>, 2013.
- 1277 Whelan, M. E. and Rhew, R. C.: Carbonyl sulfide produced by abiotic thermal and photodegradation of soil organic
1278 matter from wheat field substrate, 120, 54–62, <https://doi.org/10.1002/2014JG002661>, 2015.
- 1279 Whelan, M. E., Hilton, T. W., Berry, J. A., Berkelhammer, M., Desai, A. R., and Elliott Campbell, J.: Carbonyl
1280 sulfide exchange in soils for better estimates of ecosystem carbon uptake, 16, 3711–3726,
1281 <https://doi.org/10.5194/acp-16-3711-2016>, 2016.
- 1282 Whelan, M., Lennartz, S., Gimeno, T., Wehr, R., Wohlfahrt, G., Wang, Y., Kooijmans, L., Hilton, T., Belviso, S.,
1283 Peylin, P., Whelan, M. E., Lennartz, S. T., Gimeno, T. E., Kooijmans, L. M. J., Hilton, T. W., Commane, R., Sun,
1284 W., Chen, H., Kuai, L., Mammarella, I., Maseyk, K., Berkelhammer, M., Li, K.-F., Yakir, D., Zumkehr, A.,
1285 Katayama, Y., Ogée, J., Spielmann, F. M., Kitz, F., Rastogi, B., Kesselmeier, J., Marshall, J., Erkkilä, K.-M.,
1286 Wingate, L., Meredith, L. K., He, W., Bunk, R., Launois, T., Vesala, T., Schmidt, J. A., Fichot, C. G., Seibt, U.,
1287 Saleska, S., Saltzman, E. S., Montzka, S. A., Berry, J. A., and Campbell, J. E.: Reviews and syntheses: Carbonyl
1288 sulfide as a multi-scale tracer for carbon and water cycles, 15, 3625–3657, [https://doi.org/10.5194/bg-15-3625-](https://doi.org/10.5194/bg-15-3625-2018)
1289 [2018](https://doi.org/10.5194/bg-15-3625-2018), 2018.
- 1290 Wilhelm, Emmerich., Battino, Rubin., and Wilcock, R. J.: Low-pressure solubility of gases in liquid water, 77,
1291 219–262, <https://doi.org/10.1021/cr60306a003>, 1977.
- 1292 Wohlfahrt, G., Brilli, F., Hörtnagl, L., Xu, X., Bingemer, H., Hansel, A., and Loreto, F.: Carbonyl sulfide (COS)
1293 as a tracer for canopy photosynthesis, transpiration and stomatal conductance: Potential and limitations, 35, 657–
1294 667, <https://doi.org/10.1111/j.1365-3040.2011.02451.x>, 2012.
- 1295 Wu, J., Larsen, K. S., van der Linden, L., Beier, C., Pilegaard, K., and Ibrom, A.: Synthesis on the carbon budget
1296 and cycling in a Danish, temperate deciduous forest, 181, 94–107,
1297 <https://doi.org/10.1016/j.agrformet.2013.07.012>, 2013.
- 1298 Yan, Y., Li, R., Peng, L., Yang, C., Liu, C., Cao, J., Yang, F., Li, Y., and Wu, J.: Emission inventory of carbonyl
1299 sulfide (COS) from primary anthropogenic sources in China, 247, 745–751,
1300 <https://doi.org/10.1016/j.envpol.2019.01.096>, 2019.
- 1301 Yang, F., Qubaja, R., Tatarinov, F., Stern, R., and Yakir, D.: Soil-atmosphere exchange of carbonyl sulfide in a
1302 Mediterranean citrus orchard, 19, 3873–3883, <https://doi.org/10.5194/acp-19-3873-2019>, 2019.
- 1303 Yi, Z., Wang, X., Sheng, G., Zhang, D., Zhou, G., and Fu, J.: Soil uptake of carbonyl sulfide in subtropical forests
1304 with different successional stages in south China, 112, <https://doi.org/10.1029/2006JD008048>, 2007.



- 1305 Zeebe, R. E.: On the molecular diffusion coefficients of dissolved CO_2 , HCO_3^- , and CO_3^{2-} and their dependence
1306 on isotopic mass, 75, 2483–2498, <https://doi.org/10.1016/j.gca.2011.02.010>, 2011.
- 1307 Zhang, J., Wang, L., and Yang, Z.: Emission of Biogenic Sulfur Gases from the Microbial Decomposition of
1308 Cystine in Chinese Rice Paddy Soils Environmental Contamination and Toxicology 850, Bull. Environ. Contam.
1309 Toxicol, 850–857 pp., 2004.
- 1310 Zobler, L.: A World Soil File for Global Climate Modelling, 87802, 1986.
- 1311 Zumkehr, A., Hilton, T. W., Whelan, M., Smith, S., Kuai, L., Worden, J., and Campbell, J. E.: Global gridded
1312 anthropogenic emissions inventory of carbonyl sulfide, 183, 11–19,
1313 <https://doi.org/10.1016/j.atmosenv.2018.03.063>, 2018.
- 1314



1315



1316

1317

1318

Figure 1: Map of wetlands distribution used to represent anoxic soils in ORCHIDEE. The map resolution is 0.5°x0.5° (adapted from Tootchi et al., 2019).

1319

1320



1321 **Table 1:** lists the sites' characteristics including their identification name, location, climate, soil type, dominant
 1322 **vegetation and species, corresponding PFT fractions we used for the ORCHIDEE simulations, and reference studies for**
 1323 **more details. The spatial distribution of the sites is represented in Appendix B, Figure B1.**

	Grassland	Savannah-like grassland	Deciduous broadleaf forest	Agricultural soybean field	Evergreen needleleaf forest	Boreal evergreen needleleaf forest	Temperate deciduous broadleaf forest
Country	Austria	Spain	Denmark	Italy	Estonia	Finland	United-States
Sampling site	Neustift	Las Majadas del Tietar	Sorø	Rivignano	Järvelja	Hyttälä	Harvard
ID	AT-NEU	ES-LMA	DK-SOR	IT-CRO	ET-JA	FI-HYY	US-HA
Coordinates	47°07'N, 11°19'E	39°56'N, 5°46'W	55°29'N, 11°38'E	45°52'N, 13°05'E	58°16'N, 27°18'E	61.85°N, 24.29°E	42.54°N, 72.17°W
Climate	Humid continental	Mediterranean	Temperate maritime	Humid subtropical	Temperate	Boreal	Cool, moist temperate
Soil type	Fluvisol	Abruptic Luvisol	Alfisols or Mollisols	Silt loam	Haplic Gleysol	Haplic podzol	Sandy loam glacial till
Dominant vegetation	Graminoids: <i>Dactylis glomerata</i> , <i>Festuca pratensis</i> Forbs: <i>Ranunculus acris</i> , <i>Taraxacum officinale</i>	Tree: <i>Quercus ilex</i> Grass: <i>Vulpia bromoides</i>	European beech (<i>Fagus sylvatica</i>)	Soybean	Norway spruce (<i>Picea abies</i>)	Scots pine (<i>Pinus sylvestris</i>)	Red oak (<i>Quercus rubra</i>), Red maple (<i>Acer rubrum</i>), Hemlock (<i>Tsuga canadensis</i>).
ORCHIDEE PFT representation	100% temperate natural grassland (C ₃) (PFT 10)	20% temperate broadleaf evergreen (PFT 5) 80% temperate natural grassland (C ₃) (PFT 10)	80% boreal broadleaf summergreen (PFT 8) 20% boreal natural grassland (C ₃) (PFT 15)	100% C3 crops (PFT 12)	50% boreal needleleaf evergreen (PFT 7) 40% boreal broadleaf summergreen (PFT 8) 10% boreal natural grassland (C ₃) (PFT 15)	80% boreal needleleaf evergreen (PFT 7) 20% boreal natural grassland (C ₃) (PFT 15)	80% temperate broadleaf summergreen (PFT 6) 20% of temperate natural grassland (C ₃) (PFT 10)
References	Hörtnagl et al. (2011) Hörtnagl and Wohlfahrt (2014) Spielmann et al. (2019) Kitz et al. (2020)	Lopez-Sangil et al. (2011) El-Madany et al. (2018) Weiner et al. (2018) Spielmann et al. (2019) Kitz et al. (2020)	Pilegaard et al. (2011) Wu et al. (2013) Brændholt et al. (2018) Spielmann et al. (2019) Kitz et al. (2020)	Spielmann et al. (2019)	Noe et al. (2011, 2015) Kitz et al. (2020)	Kolari et al. (2009) Sun et al. (2018)	Urbanski et al. (2007) Wehr et al. (2017)



1325 **Table 2: Prescribed COS surface fluxes used as model input. Mean magnitudes and standard deviations of different**
1326 **types of fluxes are given for the period 2009-2016.**

Type of COS flux	Temporal resolution	Total (Gg S yr ⁻¹)	Standard deviation (Gg S yr ⁻¹)	Data Source
Anthropogenic	Monthly, interannual	394	21	Zumkehr et al. (2018). The fluxes for the year 2012 were repeated after 2012.
Biomass burning	Monthly, interannual	48	9	Stinecipher et al. (2019)
Soil	Monthly, interannual	See Table 5.	5 (oxic) 2 (anoxic)	This work, including mechanistic and empirical approaches (Berry et al., 2013; Launois et al., 2015)
Ocean	Monthly, interannual	313	14	Lennartz et al. (2021) and Masotti et al. (2015) for indirect oceanic emissions (via CS ₂ and DMS respectively), and Lennartz et al. (2017) for direct oceanic emissions
Vegetation uptake	Monthly, interannual	-576	7	Maignan et al. (2021)

1327

1328

1329 **Table 3: Comparison between simulated and measured weekly soil COS fluxes (RMSD) at ES-LMA, DK-SOR, IT-**
1330 **CRO, AT-NEU, ET-JA, FI-HYY and US-HA. Values in bold show the highest accuracy between modelled and**
1331 **measured soil COS fluxes for each site (smallest RMSD values). Soil COS fluxes are computed with a variable**
1332 **atmospheric COS concentration.**

	Empirical model	Mechanistic model
ES-LMA	3.20	4.39
DK-SOR	0.45	0.75
IT-CRO	4.45	2.58
AT-NEU	1.76	1.82
ET-JA	0.84	0.46
FI-HYY chamber 1	1.21	0.89
FI-HYY chamber 2	0.99	0.58
US-HA	3.34	1.19
Mean all sites	2.03	1.58

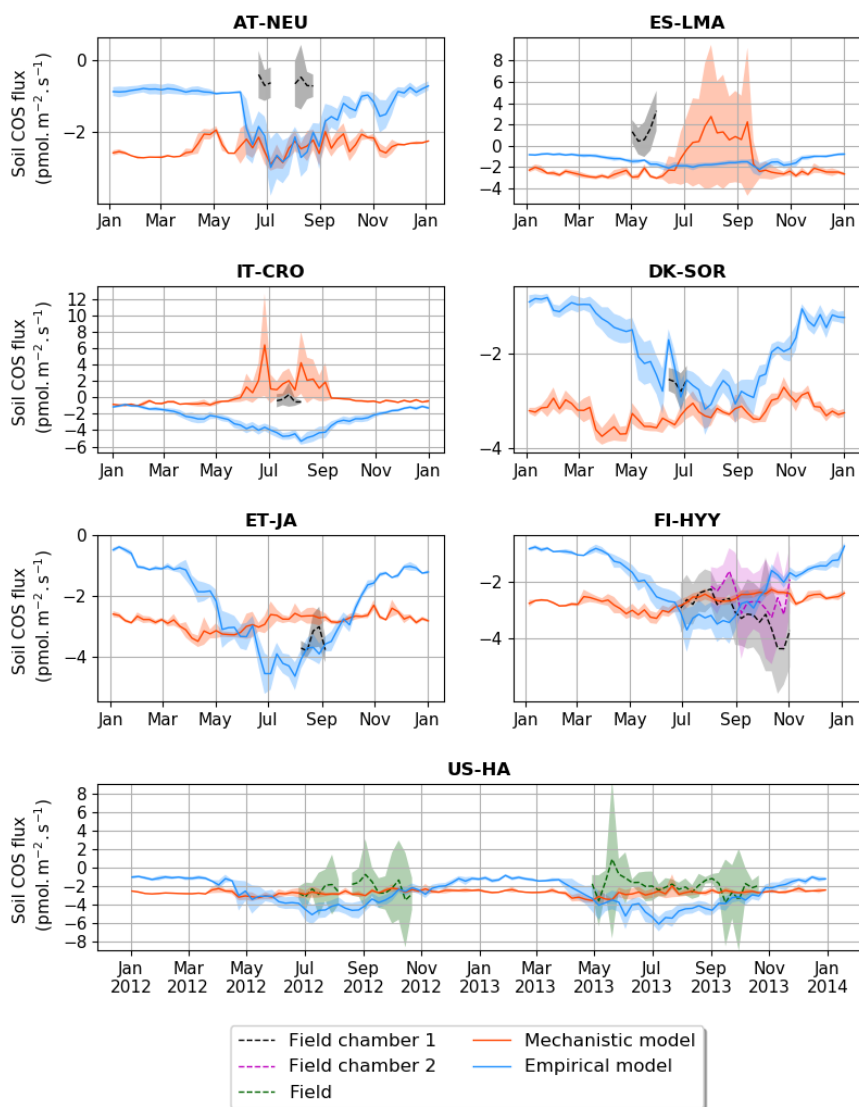


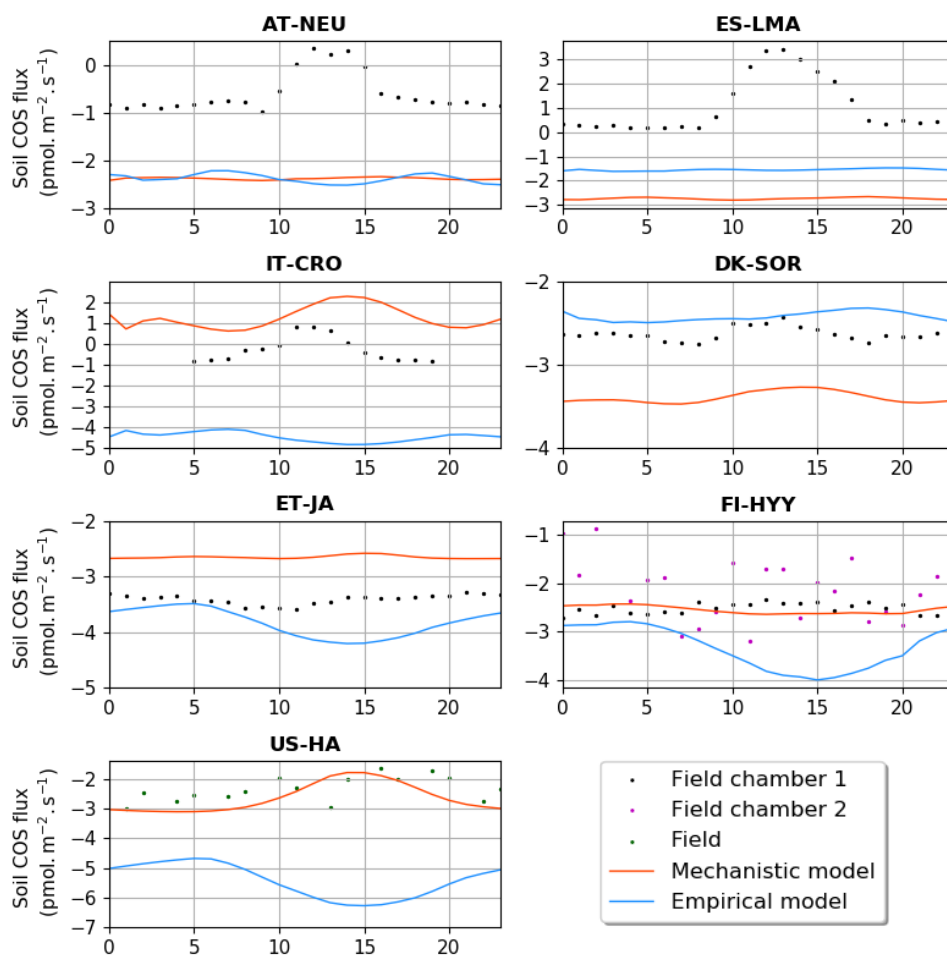
Figure 2: Seasonal cycle of weekly average net soil COS fluxes ($\text{pmol m}^{-2} \text{s}^{-1}$) at: AT-NEU, ES-LMA, IT-CRO, DK-SOR, ET-JA, FI-HYY and US-HA. The shaded areas around the observation and simulation curves represent the standard-deviation over a week for each site. Soil COS fluxes are computed with a variable atmospheric COS concentration.



1341 Table 4: Comparison between simulated and measured half-hourly soil COS fluxes (RMSD) at ES-LMA, DK-SOR, IT-
1342 CRO, AT-NEU, ET-JA, FI-HYY and US-HA. Values in bold show the highest accuracy between modelled and
1343 measured soil COS fluxes for each site (smallest RMSD values). Soil COS fluxes are computed with a variable
1344 atmospheric COS concentration.

	Empirical model	Mechanistic model
ES-LMA	2.71	3.90
DK-SOR	0.39	0.91
IT-CRO	3.82	1.33
AT-NEU	2.22	2.24
ET-JA	0.22	1.21
FI-HYY chamber 1	0.97	0.18
FI-HYY chamber 2	1.39	0.73
US-HA	3.21	0.54
Mean all sites	1.87	1.38

1345



1346

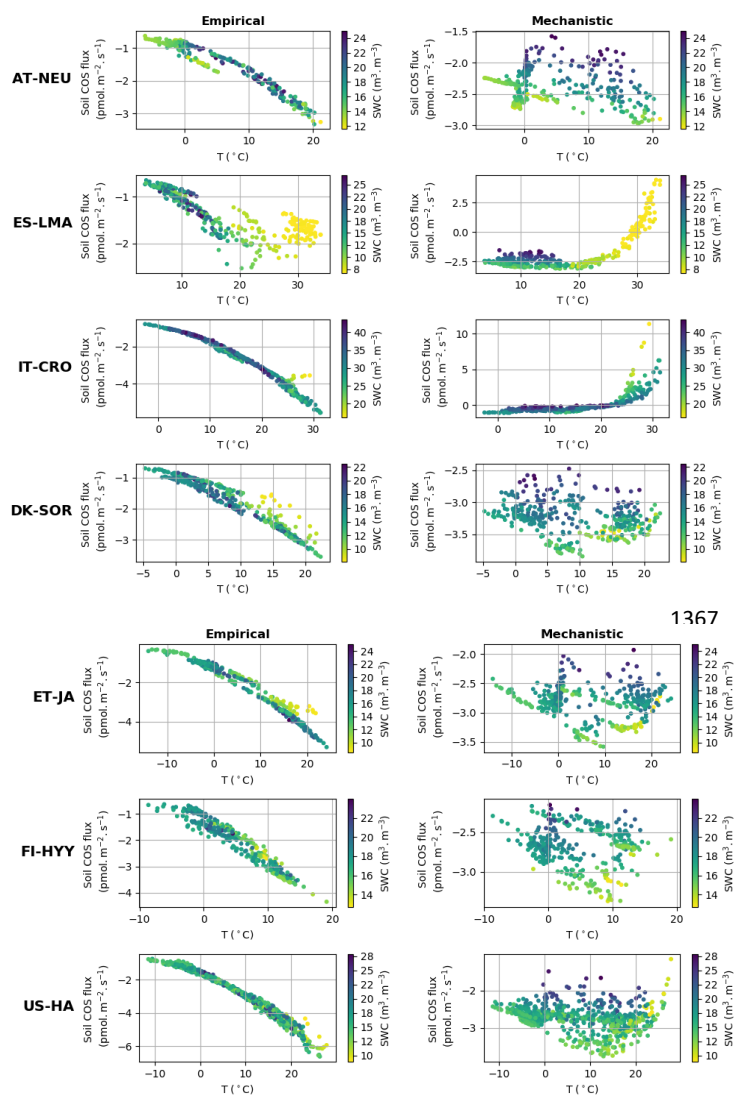
1347

1348

1349

1350

Figure 3: Mean diel cycle of net soil COS fluxes ($\text{pmol m}^{-2} \text{s}^{-1}$) over a month at: AT-NEU (08/2015), ES-LMA (05/2016), IT-CRO (07/2017), DK-SOR (06/2016), ET-JA (08/2016), FI-HYY (08/2015) and US-HA (07/2012). Soil COS fluxes are computed with a variable atmospheric COS concentration. The observation-based diel cycles (dots) are computed using Random Forest models at At-NEU, ES-LMA, IT-CRO, DK-SOR and ET-JA. At AT-NEU and ES-LMA.



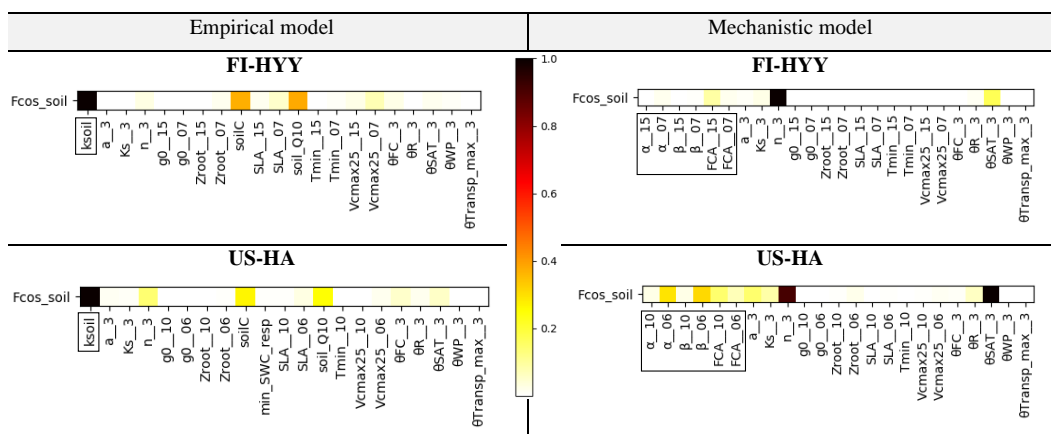
1381

1382

1383

1384

Figure 4: Simulated daily average net soil COS flux ($\text{pmol m}^{-2} \text{s}^{-1}$) versus soil temperature ($^{\circ}\text{C}$) and soil water content (SWC) ($\text{m}^3 \cdot \text{m}^{-3}$) at AT-NEU, ES-LMA, IT-CRO, DK-SOR, ET-JA, US-HA and FI-HYY, for the empirical and the mechanistic model.

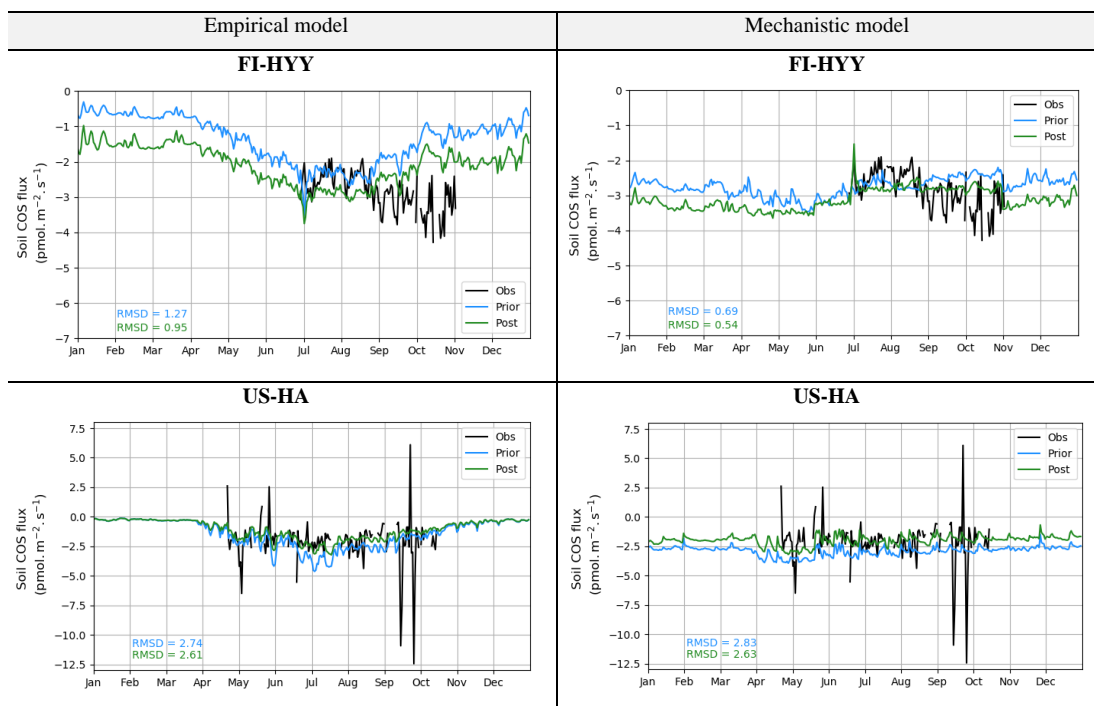


1385

1386 **Figure 5: Morris sensitivity scores of the key parameters to which soil COS fluxes are sensitive, for the empirical (left)**
 1387 **and the mechanistic (right) models. The two studied sites are FI-HYY (top) and US-HA (bottom). Full descriptions of**
 1388 **each tested parameter can be found in Tables S3 and S4 in the supporting information. The numbers at the end of the**
 1389 **parameter names correspond to the PFTs at each site for the PFT-dependent parameters, and to the dominant soil**
 1390 **texture for soil texture-dependent parameters (soil texture number 3, i.e. sandy loam, at FI-HYY and US-HA). The**
 1391 **first-order parameters are shown in the frames.**

1392

1393

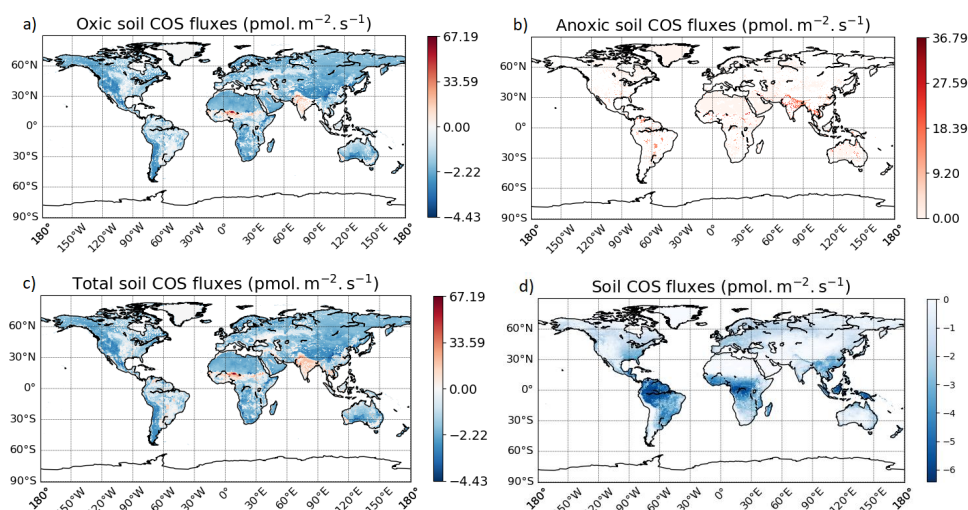


1394

1395 **Figure 6: Prior and post optimization net soil COS fluxes ($\text{pmol m}^{-2} \text{s}^{-1}$) for the empirical (left) and the mechanistic**
 1396 **(right) models. The two studied sites are FI-HYY (top) in 2015 and US-HA (bottom) in 2013.**



1397



1398

1399

1400

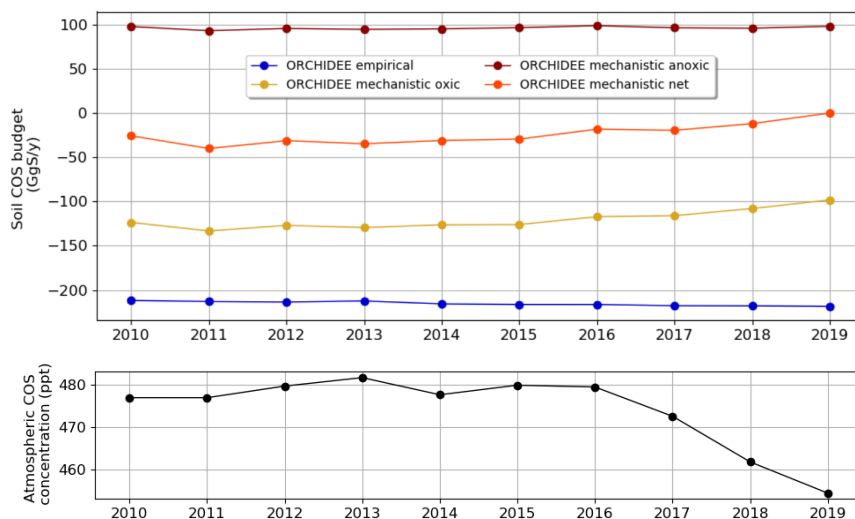
1401

1402

1403

Figure 7: Maps of mean soil COS fluxes for the mechanistic (a, b, c) and the empirical model (d), computed over 2010-2019 with a variable atmospheric COS concentration. Color scales were normalized between the minimum and maximum soil COS flux values and centered on zero for oxidic and total soil COS fluxes computed with the mechanistic model. The map resolution is 0.5°x0.5°.

1404



1405

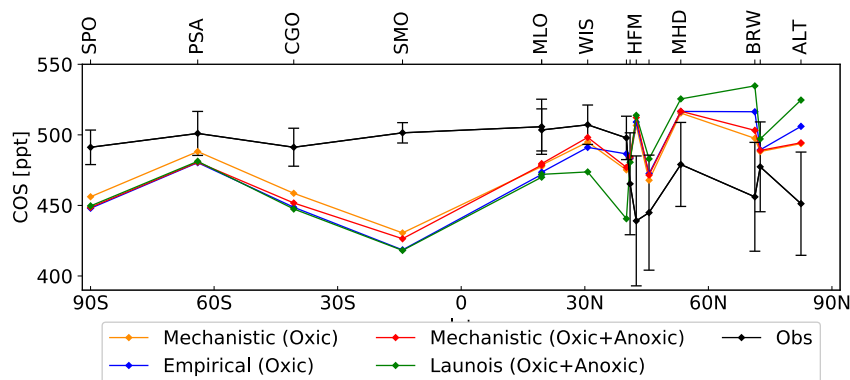
1406

1407

1408

Figure 8: Evolution of mean annual soil COS budget and mean annual atmospheric COS concentration between 2010 and 2019, computed with a variable atmospheric COS concentration.

1409

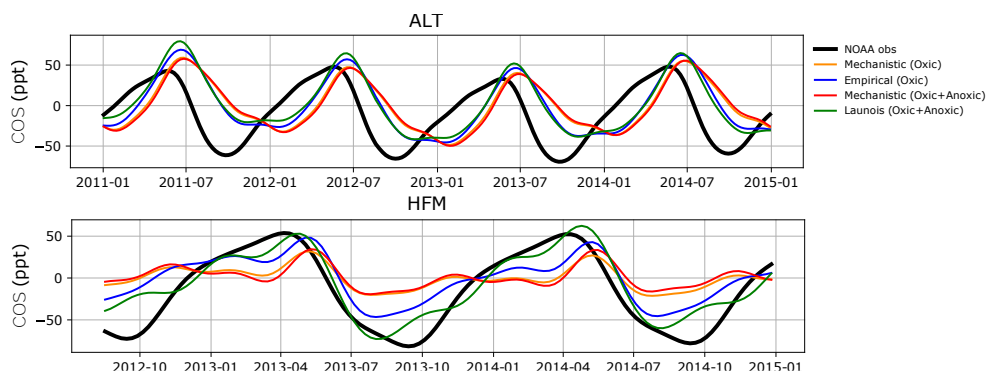


1410

1411 **Figure 9:** Comparison of the latitudinal variations of the COS abundances simulated by LMDZ at NOAA sites with the
 1412 observations (black). The LMDZ COS abundances have been vertically shifted such that the means of the simulated
 1413 concentrations are the same as the mean of the observations. The error bars around the black curve represent the
 1414 standard deviation over the whole studied period at each NOAA site. The orange curve is obtained using the oxic soil
 1415 fluxes of the mechanistic model. The red curve is obtained using the oxic and anoxic soil fluxes of the mechanistic model.
 1416 The blue curve is given by LMDZ using the oxic soil fluxes from the Berry empirical model. The green curve is obtained
 1417 using the soil fluxes from the empirical approach of Launois et al. (2015). For more clarity, the names of the stations
 1418 KUM (19.74°N, 155.01°W), NWR (40.04°N, 105.54°W), LEF (45.95°N, 90.28°W) and SUM (72.6°N, 38.42°W) are not
 1419 shown on this figure due to their proximity to other stations (Appendix B, Figure B1 and Table B1).

1420

1421



1422

1423 **Figure 10.** Detrended temporal evolution of simulated and observed COS concentrations at two selected sites, for the
 1424 mechanistic (Oxic soils alone, and Oxic + Anoxic soils) and empirical approaches (Berry et al., 2013; Launois et al.,
 1425 2015) simulated with LMDZ6 transport between 2011 and 2015. Top: Alert station (ALT, Canada), bottom: Harvard
 1426 Forest station (HFM, USA). The curves have been detrended beforehand and filtered to remove the synoptic variability
 1427 (see Sect. 2.3.3).

1428



1429 **Table 5: Comparison of soil COS budget per year (GgS yr⁻¹). The net total COS budget is computed by adding all**
 1430 **sources and sinks of COS used to transport COS fluxes (Table 2).**

	Kettle et al. (2002)	Berry et al. (2013)	Launois et al. (2015)			This study	
			ORCHIDE E	LPJ	CLM4	Empirical soil model	Mechanistic soil model
Period	2002	2002–2005	2006–2009			2009–2016	
Plants	-238	-738	-1335	-1069	-930	-576	
Soil oxic	-130	-355	-510			-214	-126
Soil anoxic	+26	Neglected	+101			Neglected	+96
Soil total	-104	-355	-409			-214	-30
Net total	+64	+1	-566	-300	-161	-35	+149

1431

1432